Water Resources Research

RESEARCH ARTICLE
10.1029/2019WR024712

Key Points:
- We developed a novel approach to model coupled fluid flow and solid mechanics in porous media with two characteristic length scales
- The model was validated against data on flow and chemically driven deformation in viscoplastic and elastic solids
- Sedimentary rock permeability is predicted to have an error function dependence on the volume fraction occupied by microporous clay

Supporting Information:
- Supporting Information S1
- Data Set S1
- Movie S2

Correspondence to:
F. J. Carrillo,
franjcf@princeton.edu

Citation:
Carrillo, F. J., & Bourg, I. C. (2019). A Darcy-Brinkman-Biot approach to modeling the hydrology and mechanics of porous media containing macropores and deformable microporous regions. *Water Resources Research*, *55*, 8096–8121. https://doi.org/10.1029/2019WR024712

Received 5 JAN 2019
Accepted 27 AUG 2019
Accepted article online 2 SEP 2019
Published online 16 OCT 2019

A Darcy-Brinkman-Biot Approach to Modeling the Hydrology and Mechanics of Porous Media Containing Macropores and Deformable Microporous Regions

Francisco J. Carrillo[1] and **Ian C. Bourg**[2]

[1]Department of Chemical and Biological Engineering (CBE), Princeton University, Princeton, NJ, USA, [2]Department of Civil and Environmental Engineering (CEE) and Princeton Environmental Institute (PEI), Princeton University, Princeton, NJ, USA

Abstract The coupled hydrology and mechanics of soft porous materials (such as clays, hydrogels, membranes, and biofilms) is an important research area in several fields, including water and energy technologies as well as biomedical engineering. Well-established models based on poromechanics theory exist for describing these coupled properties, but these models are not adapted to describe systems with more than one characteristic length scale, that is, systems that contain both macropores and micropores. In this paper, we expand upon the well-known Darcy-Brinkman formulation of fluid flow in two-scale porous media to develop a "Darcy-Brinkman-Biot" formulation: a general coupled system of equations that approximates the Navier-Stokes equations in fluid-filled macropores and resembles the equations for poroelasticity in microporous regions. We parameterized and validated our model for systems that contain either plastic (swelling clay) or elastic microporous regions. In particular, we used our model to predict the permeability of an idealized siliciclastic sedimentary rock as a function of pore water salinity and clay content. Predicted permeability values are well described by a single parametric relation between permeability and clay volume fraction that agrees with existing experimental data sets. Our novel formulation captures the coupled hydro-chemo-mechanical properties of sedimentary rocks and other deformable porous media in a manner that can be readily implemented within the framework of Digital Rock Physics.

Plain Language Summary Knowledge of how fluids flow through porous materials has significant implications for the design and operation of batteries, aquifers, oil rigs, and biomedical devices. Even though scientists have been successful in creating computer models that capture fluid flow through *rigid* porous media, it has been very challenging to create models that can model flow through *deformable* porous media. In this paper, we describe a new model that can predict flow through and around deformable porous media. We derived this model by superimposing separate conventional fluid-flow and solid-deformation models into a single simulation through a technique called volume averaging. We then connected the two models using Newton's Third Law, meaning that when fluids flow through a porous solid they "push" the solid, and whenever a solid resists fluid movement or deforms, it "pushes" the fluid in turn. The resulting model can capture complex multiscale, multiphysics phenomena such as the impact of clay swelling (think of an expanding sponge absorbing water) on the ability of fluids to flow through soils or sedimentary rock formations. Given the model's generality and its successful verification presented in this paper, we believe that it can help understand important phenomena in the fields of water and energy resources.

1. Background and Introduction

How does the permeability of sedimentary media depend on porosity, mineralogy, fluid chemistry, and stress history? This question has been a recurrent theme in subsurface hydrology for over half a century (Berg, 1970; Bourg & Ajo-Franklin, 2017; Brace, 1980; Nelson, 1994). It impacts a range of endeavors that shape humanity's energy landscape including hydrocarbon migration and recovery (Alvarado & Manrique, 2010), geothermal energy production (Barbier, 1997), geologic carbon sequestration (Klaus, 2003), and radioactive waste storage (Sellin & Leupin, 2014). The last two technologies have the potential to contribute up to half of the mitigation effort required to stabilize global CO_2 emissions (Metz et al., 2005; Socolow & Pacala, 2004) but require the ability to accurately predict the permeability evolution of ductile fine-grained sedimentary rocks (shale and mudstone) over millennial timescales in the presence of geochemical and geomechanical disturbances (Bourg & Ajo-Franklin, 2017; Neuzil, 2013).

A major challenge associated with developing a predictive understanding of flow in fine-grained sedimentary media is that these structures have two characteristic length scales: a *macroscale* defined by the assemblages of coarse grains of quartz, feldspar, or carbonate over distances of micrometers and a *microscale* defined by the assemblages of clay minerals (primarily smectite and illite) over distances of nanometers (Bourg & Ajo-Franklin, 2017). Figure 1a shows a conceptual model of the macroscale structure of sedimentary rocks as a mixture of rigid coarse grains, a deformable microporous clay matrix, and macropores (Crawford et al., 2008; Marion et al., 1992; Revil & Cathles, 1999). This model is consistent with electron microscopy observations (Nadeev et al., 2013; Nole et al., 2016; Tuller & Or, 2003) as exemplified in Figures 1b–1d (Fiès & Bruand, 1998; Peters, 2009). Experimental data indicate that permeability in fine-grained soils, sediments, and sedimentary rocks can be highly sensitive to the spatial distribution of the clay matrix (Abichou et al., 2002; Nadeau, 1998).

A second major challenge is that the microporous clay matrix is nonrigid: It can swell or shrink in response to changes in salinity and deform in response to fluid flow or external stresses in a manner that reflects the nanoscale colloidal interactions between negatively charged clay particles (Liu, 2013; Madsen & Muller-Vonmoos, 1989; Suzuki et al., 2005; Teich-McGoldrick et al., 2015). The resulting dynamics of the clay matrix give rise to significant couplings between the hydrologic, chemical, and mechanical (HCM) properties of clayey media (Carey et al., 2014; Erol, 1977; Murad & Cushman, 1997). These couplings are particularly strong if the clay fraction contains significant amounts of smectite (i.e., swelling clay minerals) and if the pore water contains predominantly sodic salts. In these cases, swelling by more than 1400% and swelling pressures up to ~50 MPa have been reported (Karnland et al., 2007; Norrish, 1954). In short, fundamental predictions of the permeability of fine-grained sediments and sedimentary rocks require a model capable of describing coupled fluid flow in pores with very different sizes (intergranular macropores and clay micropores with pore widths on the order of micrometers and nanometers, respectively) while also predicting the deformations of the microporous clay matrix induced by flow, external stresses, and salinity changes (Bourg & Ajo-Franklin, 2017).

Existing approaches to predicting the hydrology of fine-grained sedimentary media have focused on addressing either one of the two challenges outlined above but not both simultaneously. Approaches focused on the existence of two length scales have generally used an "ideal packing model" representation of clay-rich sedimentary media as a microporous (clay) medium embedded within a network of coarse grains (Crawford et al., 2008; Marion et al., 1992; Revil & Cathles, 1999). On this model, a threshold naturally emerges at a clay mineral mass fraction of ~1/3 where the microporous clay matrix becomes the load-bearing phase, in agreement with experimental observations on the core-scale hydrologic and mechanical properties of sedimentary rocks (Bourg, 2015; Crawford et al., 2008). However, existing models based on this framework invariably neglect the mechanics of the clay matrix by assuming either that the clay has a fixed porosity or that it uniformly occupies the space available within the network of coarse grains. One consequence of this approximation is that these models do not capture the influence of salinity on the permeability of clayey media (Kwon et al., 2004; Mungan, 1965; Quirk, 1986).

Conversely, approaches focused on the HCM couplings such as Terzaghi's consolidation theory, Biot's theory of poroelasticity, and Mixture Theory (theories initially developed to describe clayey media and now widely applied to other deformable porous media including hydrogels and biological tissues) simplify the governing equations for fluid and solid dynamics into a single macroscopic equation by assuming that both phases are superimposed continua with negligible inertial forces (Auton & MacMinn, 2017; Barry & Aldis, 1992; Jain & Juanes, 2009; Santillán et al., 2018; Terzaghi, 1964). This approach results in an implicitly coupled momentum equation for deformable porous media that can be paired to different body forces or solid deformation constitutive relations to create system-specific models. A drawback of this approach in the context of sedimentary rocks, however, is that it does not reflect the existence of the two characteristic length scales illustrated in Figure 1 or consequences such as the permeability threshold at a finite clay content noted above.

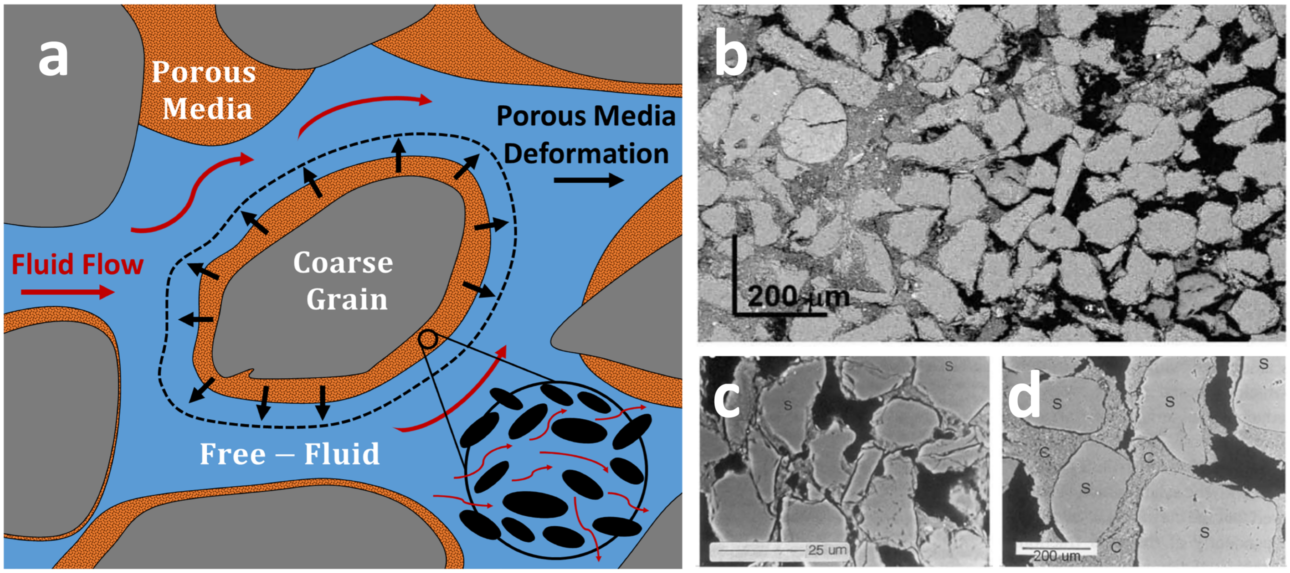

Figure 1. (a) Conceptual representation of the two key challenges posed by fluid flow in clay-rich sedimentary rocks. The structure contains three regions: rigid coarse grains, macropores, and a deformable microporous clay matrix. Fluid flow (red arrows) occurs primarily in the bulk-fluid domain, but the boundaries of this domain are influenced by the deformation of the microporous clay domain (black arrows). (b–d) Electron microscopy images of clayey media, specifically (b) a Canadian shale and (c, d) a mixture of clay and sand (denoted by the letters c and s, respectively) associated with reductive and expansive clay swelling states (Fiès & Bruand, 1998; Peters, 2009). Coarse grains, microporous clay, and macropores are shown in gray, orange, and blue in Figure 1a and in light gray, dark gray, and black in Figures 1b–1d.

The advent of Digital Rock Physics (DRP) over the last decade—that is, the combined use of X-ray computed tomography and computational methods to generate numerical models of fluid flow in real rocks (Adler et al., 1992; Fredrich, 1999; Mirabolghasemi et al., 2015; Raeini et al., 2017)—provides a potential route to simultaneously addressing both challenges outlined above. In the last few years, a handful of DRP studies have examined rocks with two characteristic length scales including fractured porous rocks, vuggy media, and clay-rich sedimentary rocks (Keller et al., 2013; Lin et al., 2016; Saif et al., 2017). In these studies, the macroscale features (coarse grains, macropores, and microporous regions) are fully resolved, while the microscale features (i.e., particles and pores within the microporous regions) are below the resolution of the X-ray computed tomography measurements. Many of these studies used a computational framework based on a pore network model with two characteristic length scales (Mehmani et al., 2013; Mehmani & Prodanović, 2014; Prodanović et al., 2015). Alternatively, at least two used an approach based on computational fluid dynamics where flow in the macropores and microporous regions were coupled through slip-flow boundary conditions and volume-averaging based on the Darcy-Brinkman formalism (Bijeljic et al., 2018; Guo et al., 2018). The resulting models demonstrate the possibility of characterizing porous media with two characteristic length scales as mixtures of three regions (as in Figure 1a) and in coupling fluid flow in the macropores and microporous regions (Golfier et al., 2015; Soulaine et al., 2017). However, these studies all assumed a static porous medium configuration, a significant limitation in the case of clay-rich media, as noted above.

Our approach combines three well established theoretical frameworks (Figure 2) to develop a simulation methodology compatible with DRP and capable of capturing both the existence of two characteristic length scales and the deformation and swelling of microporous clay in sedimentary media. To model fluid flow, we draw on the comprehensive amount of literature dedicated to volume-averaging as a way to upscale the flow velocities within micropores into an average superficial velocity that can be coupled to the macropore fluid velocity, as seen in Figure 2a (Beavers & Joseph, 1967; Brinkman, 1947; Ochoa-Tapia & Whitaker, 1995; Wang et al., 2015). Strictly speaking, Brinkman (1947) was the first to include a coupling term in the fluid momentum conservation equation to model drag in a packed bed within a macroscopic framework. This framework was later verified, formalized, and expanded through volume averaging of the fluid conservation equations within a representative elementary volume (REV; Hsu & Cheng, 1990; Ochoa-Tapia & Whitaker, 1995). In the last few years, this framework has been extended to account for moving, yet rigid, microporous regions (Wang et al., 2015) and to model dissolution dynamics in a multiscale system by

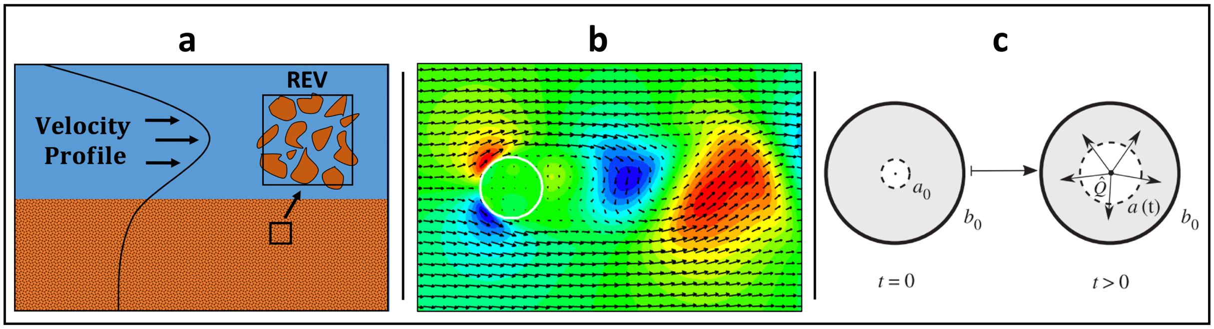

Figure 2. Illustration of the three main theoretical frameworks combined in the present study to model fluid flow in porous media with two characteristic length scales and a deformable microporous matrix: (a) models based on the Darcy-Brinkman formulation that describe coupled fluid flow in macropores (clear region) and in a microporous medium (shaded region; Ochoa-Tapia & Whitaker, 1995); (b) boundary methods that simulate flow around moving impermeable solids (Breugmem & Verzicco, 2013); and (c) poromechanics model of a cylindrical conduit where the fluid and porous solid are in a single domain (grey) and forces are imposed through boundary conditions (Auton & MacMinn, 2017). Here Q represents the fluid flow rate, and $a(t)$ and b_0 represent the inner and outer radii of the cylinder, respectively.

introducing chemical reactions at immersed boundaries (Soulaine et al., 2017, 2018; Soulaine & Tchelepi, 2016). Until now, however, no study has applied Brinkman's formalism to model coupled fluid-solid dynamics at multiple length scales in systems that include deformable microporous regions.

To describe the deformation of the boundary between macropores and microporous clay regions, we use the Brinkman framework's implicit treatment of this interface through an immersed boundary condition (Figure 2b) enforced through volume averaging and the inclusion of fluid-solid interaction terms in the momentum equations. This obviates the need for complex remeshing procedures associated with two-domain models, where solid and fluid dynamics are solved in separate regions and closure is provided by equations describing the solid-fluid interface (Batty et al., 2007; Tezduyar, 2001). Finally, to model the mechanics of the microporous clay regions, we draw on the poromechanics theories of Terzaghi (1964), Biot (1941), and others outlined above (Figure 2c).

The main contribution of this paper is the incorporation of a volume-averaged porous media dynamics equation into the modeling framework established by Brinkman, Hsu, Ochoa-Tapia, Soulaine, and coworkers. This is done by implementing concepts from coupled fluid-solid dynamics present in Terzaghi's consolidation theory, Biot's theory of poroelasticity, and Mixture Theory (Biot, 1941; Siddique et al., 2017; Terzaghi, 1964). The result is a Darcy-Brinkman-Biot modeling framework consisting of a system of differential equations (section 2) that can be numerically solved (section 3) to model HCM coupled systems with two characteristic length scales. The model is then parameterized with a focus on viscoplastic clay-rich sedimentary media (section 4) and validated against experimental results on the properties of these media (section 5). With proper parameterization, our framework should be applicable to other systems that involve coupled fluid flow in macropores and in a deformable microporous matrix such as soils (Murad & Cushman, 1996), biofilms (Vo & Heys, 2011), hydrogels (Datta et al., 2016), biological tissues (Dai et al., 2014), and fractures (Holtzman & Juanes, 2010; Noiriel et al., 2007). To illustrate this versatility, we also formulate and apply the model for cases where the microporous matrix undergoes elastic rather than viscoplastic deformation (section 6).

2. Model Derivation

Here we present the basic volume-averaging structure used to obtain the governing equations of the Darcy-Brinkman-Biot modeling framework. Although volume averaging is standard in the field, sufficient detail is provided to highlight the model's underlying assumptions and limitations.

2.1. Governing Equations for the Fluid Phase

We start the derivation with the continuum mass and momentum conservation equations for a generic fluid, where U_f is the fluid velocity, ρ_f is the fluid density, p_f is the fluid pressure, and τ_f is the fluid stress tensor. The subscripts f and s refer to fluids and solids, respectively.

$$\frac{\partial\left(\rho_f\right)}{\partial t}+\nabla\cdot\left(\rho_f\boldsymbol{U_f}\right)=0 \tag{1}$$

$$\frac{\partial\left(\rho_f\,\boldsymbol{U_f}\right)}{\partial t}+\nabla\cdot\left(\rho_f\boldsymbol{U_f}\boldsymbol{U_f}\right)=-\nabla p_f+\nabla\cdot\boldsymbol{\tau_f} \tag{2}$$

Here the stress tensor τ_f defines the rheological properties of the fluid, meaning that equations (1) and (2) can be used to model Newtonian or non-Newtonian fluids but also viscously deformable solids such as plastics or pseudo-plastics. Inclusion of gravity in equation (2) is trivial and omitted for brevity.

The next step is upscaling equations (1) and (2) through volume-averaging, which enables modeling systems with more than one phase in a defined volume. Volume averaging requires special care; in particular, it requires the existence of a well-defined REV, significantly larger than any of the subvolume features present in any phase, within which averaging can be carried out (Hassanizadeh, 1986; Hassanizadeh & Gray, 1979; Ochoa-Tapia & Whitaker, 1995; Whitaker, 2013). In the case of DRP studies of fine-grained sedimentary rocks, the typical voxel volume is on the order of 10 μm^3 (Mehmani & Prodanović, 2011). In the microporous clay matrix, this volume contains ~10^3 to 10^5 clay particles and constitutes an appropriate REV.

As in previous studies, we define two types of volume-averages: the intrinsic phase average $\widehat{X}_i$, which averages the properties of phase i over the volume of phase i, and the superficial phase average $\overline{X}_i$, which averages the properties of phase i over the REV. The two averages are related by the volume fraction occupied by phase i at the REV scale (ϕ_i):

$$\widehat{X}_i=\frac{1}{V_i}\int_{V_i}X_i dV \tag{3}$$

$$\overline{X}_i=\frac{1}{V_{\text{REV}}}\int_{V_i}X_i dV=\phi_i\,\widehat{X}_i \quad \vdots \quad \phi_i=\frac{V_i}{V_{\text{REV}}} \tag{4}$$

Volume averaging of the fluid conservation equations is carried out under the assumptions that there is no mass transfer between the solid and the fluid; there is a no-slip condition at the solid-liquid interface; there is thermodynamic equilibrium within the averaging volume; turbulence effects are negligible; the density and viscosity are constant and uniform; and there are no chemical reactions. Under these conditions, the upscaled volume-averaged equations for the fluid phase are the following (Ochoa-Tapia & Whitaker, 1995; Wang et al., 2015):

$$\frac{\partial\left(\phi_f\rho_f\right)}{\partial t}+\nabla\cdot\left(\rho_f\overline{\boldsymbol{U}}_{\boldsymbol{f}}\right)=0 \tag{5}$$

$$\frac{\partial\left(\rho_f\,\overline{\boldsymbol{U}}_{\boldsymbol{f}}\right)}{\partial t}+\nabla\cdot\left(\frac{\rho_f}{\phi_f}\overline{\boldsymbol{U}}_{\boldsymbol{f}}\overline{\boldsymbol{U}}_{\boldsymbol{f}}\right)=-\phi_f\nabla\widehat{p}_f+\nabla\cdot\overline{\boldsymbol{\tau}}_{\boldsymbol{f}}+\overline{\boldsymbol{F}}_{\boldsymbol{f}} \tag{6}$$

In equation (6), $\overline{F}_f$ is a momentum transfer term (drag) between the fluid and the solid phases that approaches zero as ϕ_f goes to 1. This term is essentially a macroscopic “filter” that approximates the forces emanating from fluid's sub-REV-scale deviations in the fluid pressure and stress terms within the microporous regions originating from fluid-solid interactions. Intrinsically averaged constants are equal to themselves; hence, their averaging symbols are removed for clarity. For an incompressible Newtonian fluid, the divergence of the stress tensor takes the form:

$$\nabla\cdot\overline{\boldsymbol{\tau}}_{\boldsymbol{f}}=\nabla\cdot\left(\mu_f\nabla\overline{\boldsymbol{U}}_{\boldsymbol{f}}+\mu_f\left(\nabla\overline{\boldsymbol{U}}_{\boldsymbol{f}}\right)^T\right) \tag{7}$$

Lastly, the fluid-solid momentum transfer term $\overline{F}_f$ can be modeled using the Ergun equation, where k is a microscale (i.e., REV scale) permeability coefficient that is a function of porosity(ϕ_f) and tends toward infinity as porosity approaches one (Ochoa-Tapia & Whitaker, 1995; Soulaine & Tchelepi, 2016; Wang et al., 2015):

$$\overline{F}_f = -\phi_f \frac{\mu_f}{k\left(\phi_f\right)}\left(\overline{\boldsymbol{U}}_{\boldsymbol{f}}-\overline{\boldsymbol{U}}_{\boldsymbol{s}}\right) - \frac{1.75\,\rho_f}{\left(150\,\phi_f^3\ k\left(\phi_f\right)\right)^{0.5}}\left(\overline{\boldsymbol{U}}_{\boldsymbol{f}}-\overline{\boldsymbol{U}}_{\boldsymbol{s}}\right)\left|\overline{\boldsymbol{U}}_{\boldsymbol{f}}-\overline{\boldsymbol{U}}_{\boldsymbol{s}}\right| \tag{8}$$

where U_s is the solid velocity. The second (nonlinear) term on the right side of equation (8) accounts for inertial effects within the porous medium. For the sake of simplicity, we assume that the Reynolds number within the microporous region is small ($Re < 1$), such that we can neglect this nonlinear term. Equations (6)–(8) then yield the following governing equation for incompressible fluid flow:

$$\frac{\partial\left(\rho_f\overline{\boldsymbol{U}}_{\boldsymbol{f}}\right)}{\partial t} + \nabla\cdot\left(\frac{\rho_f}{\phi_f}\overline{\boldsymbol{U}}_{\boldsymbol{f}}\overline{\boldsymbol{U}}_{\boldsymbol{f}}\right) = -\phi_f\nabla\widehat{p}_f + \nabla\cdot\left(\mu_f\nabla\overline{\boldsymbol{U}}_{\boldsymbol{f}} + \mu_f\left(\nabla\overline{\boldsymbol{U}}_{\boldsymbol{f}}\right)^T\right) - \phi_f\frac{\mu_f}{k\left(\phi_f\right)}\left(\overline{\boldsymbol{U}}_{\boldsymbol{f}}-\overline{\boldsymbol{U}}_{\boldsymbol{s}}\right) \tag{9}$$

Equation (9) is almost identical to that used by Soulaine et al. (2017). The main difference is that the drag term $\overline{F}_f$ is expressed here as a function of the *relative* superficial velocities of the two phases as required to model flow through a mobile microporous solid. We use the intrinsic average for fluid pressure as this most resembles experimentally measured pressures and boundary conditions.

We will use equation (9) in conjunction with a spatially distributed porosity field to model flow in both the macroporous and microporous regions. In the former, the fluid fraction is unity ($\phi_f = 1$) and k is essentially infinite, such that equation (9) approximates Navier-Stokes. Conversely, in the microporous regions ($\phi_f < 1$), k values are very small, and equation (9) approximates a form of Darcy's Law:

$$\left(\overline{\boldsymbol{U}}_{\boldsymbol{f}}-\overline{\boldsymbol{U}}_{\boldsymbol{s}}\right) = -\frac{k\left(\phi_f\right)}{\mu_f}\nabla\widehat{p}_f \tag{10}$$

To account for the influence of salinity on clay swelling, the last fluid-phase transport equation that needs to be defined is the advection-diffusion equation for a salt, which we assume acts as a tracer particle:

$$\frac{\partial\left(\phi_f\widehat{C}_x\right)}{\partial t} + \nabla\cdot\left(\widehat{C}_x\overline{\boldsymbol{U}}_{\boldsymbol{f}}\right) - \nabla\cdot\left(\phi_f D_{\mathrm{e},x}\nabla\widehat{C}_x\right) = 0 \tag{11}$$

where $\widehat{C}_x$ and $D_{\mathrm{e},x}$ are the molar concentration and effective diffusion coefficient of a given species x, respectively. A reaction term can readily be added to equation (11) to describe reactive solutes (Soulaine et al., 2017). We note that in systems where the microporous region has a relatively high permeability ($k > 10^{-6}$ m^2) the Darcy-Brinkman formulation creates a nonnegligible viscous boundary layer within the solid-fluid interface (Golfier et al., 2015) that may affect predicted solute fluxes across the interface. In systems containing Na-smectite or Illite clay, this effect should be negligible due to the very low permeability of the microporous regions ($k < 10^{-15}$ m^2), as described in section 4.1.

2.2. Governing Equations for the Solid Phase

The derivation of the governing equation for the microporous solid phase follows the same averaging principles used in the previous section, with different initial equations. Porous media exhibit a wide variety of rheological properties: Some materials, such as clays, can be viscously deformed and are modeled as plastics or pseudo-plastics while others, such as membranes, deform elastically and are modeled as elastic solids (Prevost, 1978; Rüberg & Aznar, 2016; Spearman, 2017). For simplicity, we present distinct volume-averaged equations for microporous solids with either plastic or elastic properties.

For plastic microporous media, the governing equations are analogous to those used above for the fluid, but with modified stress terms. Volume averaging was carried out as outlined by Whitaker (2013) and Crowe et al. (2011) with the following assumptions: There are no chemical reactions; individual solid grains do not change phase; the solid has a uniform constant density (ρ_s); there is thermodynamic equilibrium within the averaging volume; and sub-REV-scale deviations in the solid velocity and plastic viscosity are negligible. For convenience and solver stability, solid velocity is expressed as an intrinsic phase average:

$$\frac{\partial(\phi_s\,\rho_s)}{\partial t}+\nabla\cdot\left(\phi_s\rho_s\widehat{\boldsymbol{U}}_{\boldsymbol{s}}\right)=0 \tag{12}$$

$$\frac{\partial\left(\phi_s\rho_s\widehat{\boldsymbol{U}}_{\mathbf{s}}\right)}{\partial t}+\nabla\cdot\left(\phi_s\rho_s\widehat{\boldsymbol{U}}_{\boldsymbol{s}}\widehat{\boldsymbol{U}}_{\mathbf{s}}\right)=\phi_s\nabla\cdot\widehat{\boldsymbol{\tau}}_{\boldsymbol{T}}+\phi_s\nabla\cdot\widehat{\boldsymbol{\tau}}_{\mathbf{s}}+\overline{\boldsymbol{F}}_s \tag{13}$$

The three terms on the right side of equation (13) represent pressure, internal stress, and drag contributions to the microporous solid's momentum.

For consistency with poromechanics theory, the pressure term in equation (13) is represented as a Terzaghi stress tensor ($\widehat{\tau}_{\mathrm{T}}$) that describes the effective stress on the solid as a function of confining pressure σ_{conf}, pore fluid pressure p_f, and swelling (i.e., disjoining) pressure p_{swell}:

$$\widehat{\boldsymbol{\tau}}_{\mathbf{T}}=\widehat{\boldsymbol{\sigma}}_{\boldsymbol{conf}}-\widehat{p}_f\boldsymbol{I}-\widehat{p}_{swell}\boldsymbol{I} \tag{14}$$

The terms in equation (14) have the same meaning as in standard poromechanics theory (Murad & Cushman, 1997) and enable modeling HCM-driven deformations in the microporous region. The swelling pressure term p_{swell} can be tuned to different types of swelling behavior as demonstrated in section 4. In the absence of confining and swelling pressure, $\widehat{\tau}_{\mathrm{T}}$ becomes the intrinsic fluid pressure. For simplicity, equation (14) implicitly assumes that the Biot coefficient is equal to 1, that is, it assumes a perfect transfer of pressure between the fluid and solid components. If necessary, the addition of a nonunity Biot coefficient into this expression is trivial.

For a compressible plastic, the divergence of the stress tensor is defined as follows:

$$\nabla\cdot\widehat{\boldsymbol{\tau}}_{\mathbf{s}}=\nabla\cdot\left(\mu_s^{eff}\left(\nabla\widehat{\boldsymbol{U}}_{\boldsymbol{s}}+\left(\nabla\widehat{\boldsymbol{U}}_{\mathbf{s}}\right)^T-\frac{2}{3}\nabla\cdot\left(\widehat{\boldsymbol{U}}_{\mathbf{s}}\,\boldsymbol{I}\right)\right)\right) \tag{15}$$

where the effective solid viscosity μ_s^{eff} can be described using various non-Newtonian plastic viscosity models such as the Herschel-Bulkley, Power Law, Bird-Carreau, Casson, or Spearman models (Spearman, 2017). Finally, conservation of momentum dictates $\overline{F}_s=-\overline{F}_f$, such that the complete volume-averaged momentum conservation equation for a plastic microporous solid is as follows:

$$\begin{aligned}\frac{\partial\left(\phi_s\rho_s\widehat{\boldsymbol{U}}_{\mathbf{s}}\right)}{\partial t}+\nabla\cdot\left(\phi_s\rho_s\widehat{\boldsymbol{U}}_{\boldsymbol{s}}\widehat{\boldsymbol{U}}_{\boldsymbol{s}}\right)&=\phi_s\nabla\cdot\left(\widehat{\boldsymbol{\sigma}}_{\boldsymbol{conf}}-\widehat{p}_f\boldsymbol{I}-\widehat{p}_{swell}\boldsymbol{I}\right)\\&\quad+\phi_s\nabla\cdot\left(\mu_s^{eff}\left(\nabla\widehat{\boldsymbol{U}}_{\boldsymbol{s}}+\left(\nabla\widehat{\boldsymbol{U}}_{\mathbf{s}}\right)^T-\frac{2}{3}\nabla\cdot\left(\widehat{\boldsymbol{U}}_{\mathbf{s}}\,\boldsymbol{I}\right)\right)\right)-\phi_f\frac{\mu_f}{k\left(\phi_f\right)}\left(\overline{\boldsymbol{U}}_{\mathbf{s}}-\overline{\boldsymbol{U}}_{\boldsymbol{f}}\right)\end{aligned} \tag{16}$$

Note that we neglect the inertial terms in $\overline{F}_s$, just as we did in equation (9)

For systems where the microporous solid is an isotropically linear elastic solid (rather than a plastic one), the inertial and viscosity terms in equation (13) are replaced by appropriate volume-averaged displacement and elastic deformation terms, respectively:

$$\frac{\partial^2(\phi_s\rho_s\widehat{\boldsymbol{u}}_{\boldsymbol{s}})}{\partial t^2}-\nabla\cdot\left(\phi_s\mu_s\nabla\widehat{\boldsymbol{u}}_{\boldsymbol{s}}+\phi_s\mu_s(\nabla\widehat{\boldsymbol{u}}_{\boldsymbol{s}})^T+\phi_s\lambda_s tr(\nabla\widehat{\boldsymbol{u}}_{\boldsymbol{s}})I\right)=\phi_s\nabla\cdot\widehat{\boldsymbol{\tau}}_{\boldsymbol{T}}+\overline{\boldsymbol{F}}_{\mathbf{s}} \tag{17}$$

where u_s is the solid displacement vector (not to be confused with solid velocity U_s in equation (16)) and μ_s and λ_s are the Lamé coefficients (Jasak & Weller, 2000). This form of the equations assumes small deformations and Hookean elasticity but can be expanded in a straightforward manner to include large deformations and non-Hookean dynamics (Rüberg & Aznar, 2016; Tuković & Jasak, 2007). The fluid-solid momentum exchange term ($\overline{F}_s$) and the Terzaghi stress term ($\widehat{\tau}_{\mathrm{T}}$) are the same as in equation (13). A full derivation of equations (16) and (17) is provided in the supporting information (SI).

The solid stresses at the interface are treated in a manner consistent with previous studies (Badia et al., 2009; Showalter, 2010), where by assuming continuity of stresses (i.e., conservation of momentum) we state that the solid stresses must be balanced by the fluid stresses at the interface.

$$\nabla\cdot\overline{\boldsymbol{\sigma}}_{\boldsymbol{s}} = \nabla\cdot\overline{\boldsymbol{\sigma}}_{\boldsymbol{f}}^{transferred} = \phi_s\nabla\cdot\widehat{\boldsymbol{\tau}}_{\boldsymbol{T}} + \overline{\boldsymbol{F}}_{\boldsymbol{s}} \tag{18}$$

In equation (18), σ_i represents the viscous (or elastic) stress tensor of phase i and the superscript is used to indicate that not all fluid stresses are transferred into the solid. Note that the previous equation is simply a restatement of equation (16) or (17) without the inertial terms. There are two fluid contributions to these transferred stresses: the Terzaghi stress tensor (i.e., fluid pressure and confining stresses) and the force term $\overline{\boldsymbol{F}}_{\boldsymbol{s}}$ (also defined as the fluid's volume-averaged stresses transferred to the solid). Although these are approximated averaged terms, both of them (and thus equation (18)) are valid throughout the interface and in both fluid ($\phi_s = 0$) and porous domains ($\phi_s > 0$; Neale & Nader, 1974). The main assumption is that these two terms account for the complete momentum transfer from the fluid to the solid.

Furthermore, by nature of volume averaging the solid momentum equation, both the transferred stresses and solid viscous (or elastic) stress terms become negligible in the free fluid domain ($\phi_s = 0$). This is equivalent to setting the solid's viscosity (or elasticity) to zero right outside the interface, essentially removing any solid-solid interactions between the microporous and free fluid domains. The result is that the solid stresses at the interface come only from the balance of the transferred fluid stresses.

2.3. Comparison With Biot Theory

If we simplify equation (16) or (17) by applying the assumptions present in Biot theory (i.e., stress equilibrium within the solids, no subvolume variations, no inertial effects, and no swelling pressure) and combine it with the fluid-phase approximation of Darcy's law (equation (10)), we obtain the main equation used in Biot theory:

$$\nabla\cdot\overline{\boldsymbol{\sigma}}_{\boldsymbol{s}} = \nabla\widehat{p}_f = -\frac{\mu_f}{k\left(\phi_f\right)}\left(\overline{\boldsymbol{U}}_{\boldsymbol{f}} - \overline{\boldsymbol{U}}_{\boldsymbol{s}}\right) \tag{19}$$

Overall, the model framework proposed here consists of equations (5) and (9) for the fluid phase combined with equations (12) and (16) or (17) for the microporous solid. This framework is consistent with the Navier-Stokes equations in the bulk fluid region and with Darcy's law (equation (10)) and poroelasticity theory (equation (19)) in the microporous region. The description of the microporous region is analogous to that used in Mixture Theory, where equations (5) and (10) are combined with a solid-phase momentum equation in order to obtain a Biot-like system of equations (Auton & MacMinn, 2017; Bertrand et al., 2016; Santillán et al., 2018; Siddique et al., 2017). Our overall approach, based on volume averaging of the fundamental conservation equations, incorporates the deformation of the microporous solid through an implicit approximation of the fluid-solid interface as a continuous interpolation of the fluid properties of each region (Ehrhardt, 2010; Ochoa-Tapia & Whitaker, 1995; Wang et al., 2015). For the sake of simplicity, the equations presented above were derived under the assumption that the microporous matrix exhibits either purely elastic or viscoplastic behavior. Extension of this framework to capture more complex irreversible processes such as the brittle-to-ductile transition, or rock failure would require incorporating more complex volume averaged solid-deformation constitutive equations through the approach outlined above.

The approach presented here is but one of several possible approaches toward modeling fluid-porous interface coupling. A closely related alternative is based on domain decomposition techniques whereby the fluid and porous domains are solved separately and then matched at the interface through a Beavers-Joseph type boundary condition (Beavers & Joseph, 1967; Nield, 2009). The implementation of this boundary condition in the context of a moving elastic solid has been realized in several papers (Badia et al., 2009; Showalter, 2010, and references within). This approach may allow for a more physical description of the interface by enabling the definition of a fluid velocity slip coefficient at the boundary between bulk fluid and microporous regions. However, the value of this slip coefficient is usually unknown and impractical to obtain. Furthermore, the implementation of these approaches often involves the creation of separate moving solution domains (meshes) and the coupling of separate codes, leading to a high barrier of entry. In contrast, the Darcy-

Brinkman-Biot approach only requires a single mesh and is easily implemented into conventional fluid-flow solvers by modification of the fluid momentum equation (equation (9)) and the addition of two additional equations: equations (12) and (16) or (17).

3. Computational Implementation

Equations (5), (9), (11), (12), and (16) or (17 for elastic solids) were discretized and solved in OpenFOAM (Open Source Field Operation and Manipulation), a free, widely used, open-source computational fluid dynamics C++ library (Weller & Tabor, 1998). OpenFOAM uses the Finite Volume Method, an intrinsically conservative numerical scheme, to sequentially solve discretized partial differential equations. Fluid incompressibility was enforced through a combination of the SIMPLE (Semi-Implicit-Method-of-Pressure-Linked-Equations) and PISO (Pressure-Implicit-Split-Operator) algorithms called PIMPLE, meaning that time stepping was done semi-implicitly. As appropriate for our low Mach numbers simulations, we used the pressure-velocity coupling imposed by the fluid momentum and continuity equations to enforce incompressibility through the solution of a Poisson pressure equation. Our complete algorithm was developed through the modification and expansion of the "pimpleFoam" and "solidDisplacementFoam" numerical algorithms present in OpenFOAM Version 4.0.

It is important to note that the fluid velocity field is not strictly solenoidal in the microporous medium during swelling or shrinking (i.e., $\nabla\cdot\overline{U}_f = 0$ only if $\partial\phi_s/\partial t = 0$). Therefore, it is necessary to add a correction term equal to $\partial\phi_f/\partial t$ into the PISO algorithm during the pressure-correction step. The fluid and solid equations are solved in a sequential manner within the same time step, meaning that the momentum exchange term ($\overline{\boldsymbol{F}}_{\boldsymbol{f}}$) for the fluid momentum equation is solved explicitly using values from the previous time step, while said term for the solid momentum equation is solved semi-implicitly with values from the current time step (Figure S4). This creates a loss of accuracy of same order as the time discretization scheme and, thus, a time-step restraint.

The sequential solving of the fluid and solid equations creates an inconsistency in the calculation of salt advection when solving the solid continuity equation. A correction term $\nabla\cdot\left(\widehat{C}_x\phi_s\widehat{U}_s\right)$ was added on the right side of equation (11) to ensure a correct solution (please refer to the SI for an in-depth discussion of this term). Due to the explicit nature of these errors, they can be further reduced by imposing that the timescale of solid deformation is smaller than that of fluid flow. We ensured this by implementing a protocol for variable time-stepping enforced through the restriction of Courant Numbers for both phases. In the simulations presented below, mass conservation was better than 99.99% on the fluid, solid, and salt.

The governing equations were discretized through the following methods: Time stepping was done through forward Euler; spatial discretization was done through the Gauss linear interpolation method except for the advection terms in the species conservation equations, which were discretized through a Van Leer limiter scheme. To prevent unphysical behavior in unstable systems where the timescale of solid deformation is comparable to fluid's, we added numerical dissipation to the discretized solid velocity gradient through a flux limiter on the inertial and stress terms of equation (16).

The simulations presented here were carried out in parallel on 4 to 16 Broadwell Xeon cores on Princeton's 320-node Dell Beowulf cluster. The expended CPU time was on the same order as during standard incompressible flow simulations, where the most time-consuming step consists in implicitly solving the elliptic fluid pressure equation required to enforce fluid incompressibility. For all simulations, we modified grid resolution to ensure grid-independent convergence.

4. Parametrization to Porous Media: Na-Smectite Clay

4.1. Parametrization of the Permeability Function

As noted in the introduction, a key challenge in subsurface hydrology is the strong influence of clay minerals on fluid flow in sedimentary rocks (Bourg & Ajo-Franklin, 2017). This challenge is particularly profound in systems that contain smectite clay, a microporous material whose permeability, swelling pressure, and plastic rheology are highly sensitive to porosity and aqueous chemistry (Aksu et al., 2015; Mondol et al., 2008; Spearman, 2017). Smectite is the predominant clay mineral in many unconsolidated sediments, in bentonite (a mixture of sand and clay used in geotechnical applications), and in soils formed in temperate weathering environments (Abichou et al., 2002; Sposito, 2008). Smectite and Illite clay minerals constitute roughly half of the world's sedimentary rock mass, with Illite being generally more abundant on a mass basis but both clay minerals being roughly equally important on a surface area basis. The present section parameterizes the set of equations derived above for systems where the microporous matrix consists entirely of smectite by choosing the appropriate permeability, salt diffusion, swelling pressure, and rheology models. We focus on conditions where aqueous chemistry is dominated by sodic salts such as NaCl, where smectite swelling and rheology have been most extensively characterized. The result is a closed, fully coupled system of equations.

First, we define the permeability of the clay matrix (k), the key variable that determines the sub-REV-scale momentum interaction between water and clay. For simplicity, we use the well-known Kozeny-Carman relation:

$$k\left(\phi_f\right) = \frac{1}{b\,t^2 a_s^2}\,\frac{\phi_f^3}{\left(1-\phi_f\right)^2} \tag{20}$$

Equation (20) describes the permeability of a bundle of capillary tubes of uniform radius within an impermeable solid, where b is a pore shape factor, t is the tortuosity of the pore network, and a_s is the specific surface area expressed as the ratio of surface area to solid volume (Bourg & Ajo-Franklin, 2017). The parameter values used in applying equation (20) to Na-smectite and Illite are summarized in Table 1. The shape factor was set to $b = 3 \pm 1$ based on empirical observations in a range of porous media (Bourg & Ajo-Franklin, 2017). Tortuosity was set to $t^2 = 4.0 \pm 1.6$ based on measurements of water tracer diffusion in compacted Na-smectite (Bourg et al., 2006). The specific surface area was set to 1.7 ± 0.2 nm^{-1} for smectite and 0.21 ± 0.03 nm^{-1} for illite based on experimental values reported in previous studies ($a_s = 703 \pm 60$ m^2/g for smectite and $a_s = 78 \pm 10$ m^2/g for illite, converted to units of area per volume using grain densities of $2{,}400 \pm 140$ kg/m^3 and $2{,}700 \pm 70$ kg/m^3, respectively; Brooks, 1955; Diamond & Kinter, 1956; Mesri & Olson, 1971; Orchiston, 1954; Quirk, 1955). The values of specific surface area used here are based on methods that probe the entire water-accessible surface area of clay particles, including glycerol and ethylene glycol monoethyl ether retention techniques but not standard N_2 adsorption techniques (Diamond & Kinter, 1956; Tournassat et al., 2015).

A well-known limitation of equation (20) is that it does not capture the influence of pore-sized heterogeneity (Bourg & Ajo-Franklin, 2017; Dixon et al., 1999) and, therefore, does not accurately predict the macro-scale permeability of clay-rich soils or sedimentary rocks (Mondol et al., 2008; Ren et al., 2016). The comparison with experimental data in Figure 3a, however, indicates that equation (20) provides a reasonable permeability model for pure Na-smectite and illite without the need for fitting parameters.

Two important features of the permeability of pure clay are not described by equation (20). First, the permeability data in Figure 3a relate exclusively to sodium-exchanged clays. Other data indicate that smectite (and, to a smaller extent, illite) has a higher permeability at the same porosity values if equilibrated with calcium or potassium electrolytes (Mesri & Olson, 1971). This permeability difference likely reflects the less uniform pore-sized distributions of K- and Ca-smectite (relative to Na-smectite) that results from the stronger charge-screening capacity of K and Ca ions at the clay surface. Second, clay-water mixtures exposed to one-dimensional consolidation are known to develop a textural anisotropy that makes their permeability tensor anisotropic (Hicher et al., 2017). Overall, equation (20) is used here as a simple, yet reasonably accurate permeability model in the range of conditions of interest, that is, fully saturated Na-smectite or illite in the absence of excessive anisotropy. Modifications to account for clay anisotropy, other clay counterions (such as calcium or potassium), and multiphase flow effects (e.g., the Klinkenberg Effect; Guo et al., 2018) or to implement other permeability models (Chapuis & Aubertin, 2003; Samarasinghe et al., 1982) can be readily carried out within the present framework.

4.2. Parametrization of the Swelling Pressure Term

Second, we define the swelling pressure of the microporous clay matrix. For this, we use the well-known Derjaguin-Landau-Verwey-Overbeek (DLVO) theory of colloidal interactions. More precisely, we use a

Table 1
Symbols and Values for Model Parameters

	Parameter	Symbol	Value
Basic Constants	Water density	ρ_f	1,000 kg/m^3
	Water viscosity	μ_f	1.1×10^{-3} Pa s
	Smectite clay density	ρ_s	2,400 kg/m3
	Aqueous diffusivity of Sodium Chloride	D_{NaCl}	1.2×10^{-9} m^2/s^1
Permeability Model	Permeability shape factor	b	3.0
	Clay tortuosity	t^2	4.0
	Illite specific surface area	a_s	2.1×10^8 m^{-1}
	Smectite specific surface area	a_s	1.9×10^9 m^{-1}
Clay Swelling Pressure Model	Hamaker constant for clay-water systems	A_h	2.2×10^{-20} J
	Clay aggregate (tactoid) thickness	D_p	5.2×10^{-9} m
	Swelling pre-exponential factor	S	5.8×10^8 Pa
	Swelling decay length	l	2.0×10^{-10} m
Clay Rheology Model	Reference kinematic yield stress	τ^*	0.29 m^2/s^2
	Structural parameter	β	8.0
	Fractal dimension	D	2.9
	Structural break-up constant	m	0.4
	Maximum solid fraction	ϕ_s^{max}	0.65
Elastic Solid Simulation Parameters	First Lame coefficient	μ_s	210 Pa
	Second Lame coefficient	λ_s	110 Pa
	Permeability	k_0	10^{-9} m^2
	Applied pressure	p	100 Pa

Note. Parameter values were obtained from Bourg et al. (2006), Diamond and Kinter (1956), Liu (2013), Mesri and Olson (1971), and Spearman (2017) and are consistent across the simulations unless specified otherwise.

semiempirical formulation proposed by Liu (2013) for the disjoining pressure in a water film of thickness "h" between clay tactoids (i.e., stacks of clay particles separated by ≤3 water layers):

$$p_{swell} = 2\widehat{C}_{NaCl}RT\cosh(y_m - 1) - \frac{A_h}{6\pi}\left(\frac{1}{h^3} - \frac{2}{(h + D_p)^3} + \frac{1}{(h + 2D_p)^3}\right) + S_0\exp\left(-\frac{h}{l}\right); \tag{21}$$

In equation (21), the first term on the right side is Langmuir's model (Kemper & Quirk, 1972; Langmuir, 1938) of the osmotic swelling pressure caused by overlapping electrostatic double layers in a slit-shaped nanopore, where $\widehat{C}_{NaCl}$ is the salt concentration in mol/m^3, R is the ideal gas constant (8.31446 J K^{-1} mol^{-1}), T is the temperature in Kelvin, and y_m is the scaled electrostatic potential at the midplane of the nanopore, calculated here using the so-called "compression approach" for solving the Poisson-Boltzmann equation between two charged parallel plates in a symmetrical electrolyte solution (Liu & Neretnieks, 2008). The salinity dependence of y_m gives rise to the well-known salinity dependence of clay swelling. The second term is the contribution of London dispersion forces to the swelling pressure modeled through Hamaker's approach (Hamaker, 1937), where D_p is the thickness of clay tactoids and A_h is Hamaker's constant for clay tactoids separated by a water film. The third term is an empirical description of the short-range "hydration repulsion" between clay particles, where S_0 and l are empirical coefficients. Parameter values and the relation between ϕ_f and h were taken from Liu (2013) and are listed in Table 1. Equation (21) as parametrized by Liu (2013) is used here as a convenient parametric fit to experimental data on smectite swelling as a function of ϕ_f and C.

We note that equation (21) makes significant simplifications and approximations. For example, the hydration repulsion term is purely phenomenological, while the optimal formulation and parameterization of the London dispersion term is still unsettled in the case of smectite clay (Gilbert et al., 2015; Tester et al.,

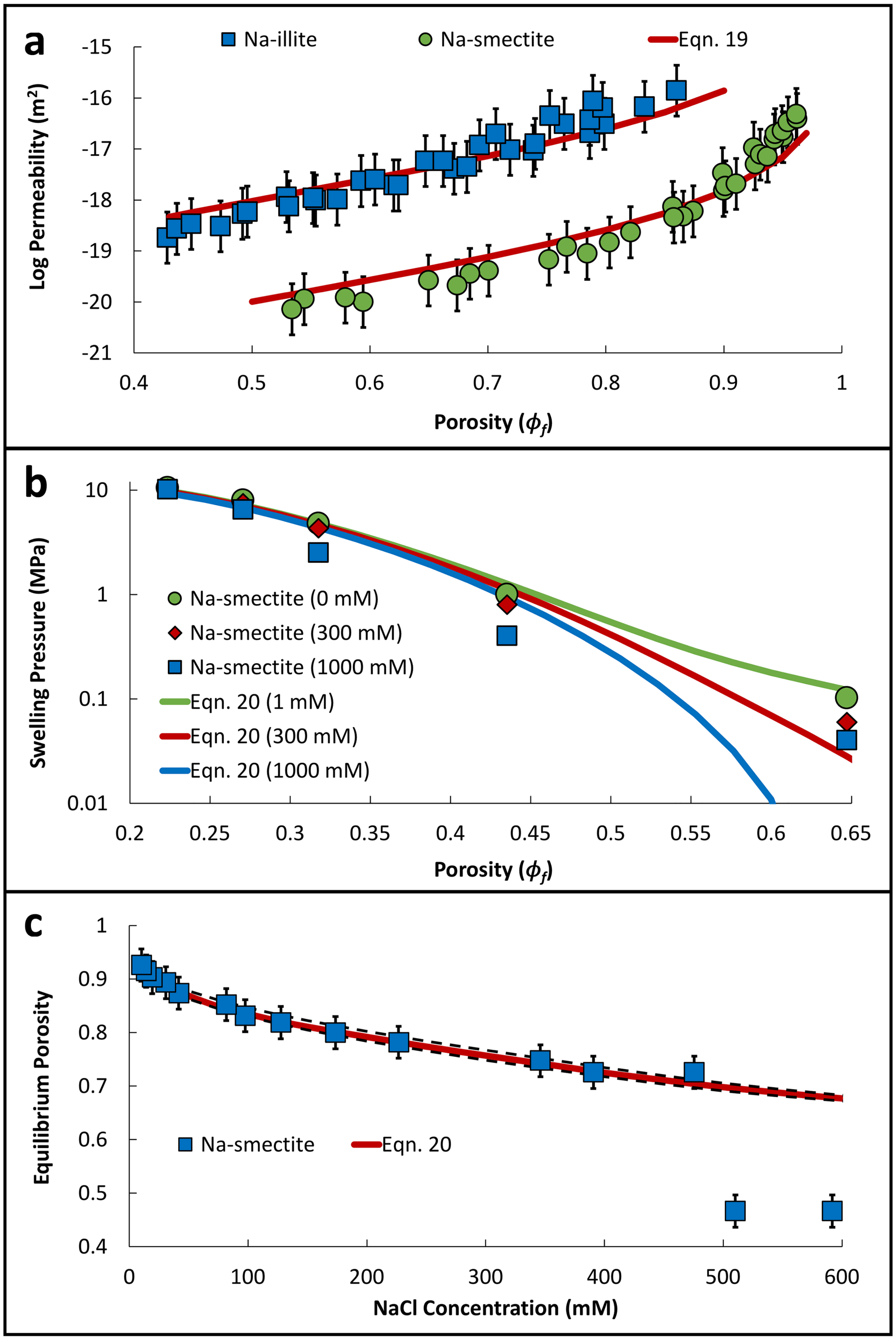

Figure 3. (a) Permeability of compacted Na-smectite and illite as a function of porosity; (b) swelling pressure of compacted bentonite as a function of porosity at different salinities (error bars are smaller than the symbols); and (c) porosity of Na-smectite as a function of salinity at a small constant confining pressure. Symbols are experimental results (Mesri & Olson, 1971; Norrish, 1954). Lines are model predictions obtained using equations (20) and (21) with no fitting parameters in Figures 3a and 3b and with a single fitting parameter (the unspecified small confining pressure used in the experiments, which was set to 0.03 MPa; dashed lines show the sensitivity of the model predictions to ±0.01-MPa differences in this value) in Figure 3c. Confidence intervals on all experimental values were roughly estimated as described in the supporting information.

2016). In addition, the first two terms in equation (21) are based on mean-field theories, that is, they neglect short-range interactions between water, ions, and clay surfaces (McBride, 1997; Missana & Adell, 2000). In the case of Na-smectite, this last approximation is valid only at interparticle distances greater than 3 nm (i.e., $\phi_f > 0.75$; Adair et al., 2001). One consequence of this is that DLVO theory does not predict the existence of stable "crystalline" swelling states with interparticle distances ≤1 nm that predominate at high salinity, high compaction, or in aqueous chemistries dominated by divalent ions (Bourg & Ajo-Franklin, 2017; Pashley & Israelachvili, 1984). Furthermore, this formulation assumes that clay swelling pressure is controlled by a single microstructural variable (interparticle distance h or, equivalently, porosity ϕ_f); more complex formulations have been proposed in the case of other microporous media with a deformable solid skeleton, such as activated carbon or zeolites (Pijaudier-Cabot et al., 2011). Finally, the numerical method used by Liu (2013) to evaluate y_m cannot be applied when $C = 0$; for simplicity we use $C = 0.001$ M as an approximation when calculating p_{swell} in pure water (resulting in a ~0.05% error in said value).

To test the accuracy of equation (21) as parameterized by Liu (2013), we used macroscopic data on the swelling pressure of confined water-saturated Na-smectite as a function of compaction and salinity (Figure 3b) as well as X-ray diffraction measurements of h versus salinity (Figure 3c). Figure 3 shows that equation (21) overestimates porosity at salinities ≥0.5 M NaCl where crystalline swelling predominates but accurately predicts experimental data at other conditions.

4.3. Parametrization of the Diffusion Coefficient

Third, we define the effective diffusion coefficient of dissolved salt (x) in the microporous clay using a form of Archie's law (Blum et al., 2007; Boving & Grathwohl, 2001):

$$D_{e,x} = \phi_f^n D_x \tag{22}$$

Although there does not exist a universal Archie's law exponent n for all porous media, several studies have concluded that a value of 2.2 to 2.5 reasonably reproduces the diffusion of ions in pure compacted clay (Revil et al., 2011; Shen & Chen, 2007; Van Loon, 2015; Van Loon et al., 2003).

Equation (22) is known to oversimplify salt diffusion in clayey media, particularly by neglecting the salinity-dependence of $D_{e,x}$ that arises from anion repulsion in the electrical double layer on charged clay surfaces (Malusis et al., 2003; Sherwood & Craster, 2000; Van Loon et al., 2004, 2007). A notable alternative to equation (22) that accounts for this effect is Kemper's model (Kemper & Rollins, 1966; Kemper & van Schaik, 1966).

$$D_{e,x} = \frac{1-e^{-y_m}}{t^2} D_x \tag{23}$$

where t is tortuosity as in equation (20), y_{m} is the same as in equation (21), and "$1-e^{-y_m}$" is the equilibrium ratio between anion concentration in the clay nanopores and in bulk liquid water. Equation (23) is less empirical than equation (22) and more consistent with the permeability and swelling pressure models used above. However, its use would require a more complex treatment of the coupled advection and diffusion of ions in equation (11), where the impact of anion exclusion is neglected. We note that multiphase flow effects such as Knudsen diffusion are neglected here due to the fact that we focus exclusively in fully water-saturated media (Malek & Coppens, 2003). Equation (22) is therefore used here for simplicity.

4.4. Parametrization of Clay Rheology

Lastly, we define the effective viscosity of the microporous clay in a manner that accounts for the impact of clay swelling and shearing on its plastic viscosity and critical shear stress (Güven, 1993; Maciel et al., 2009). Spearman (2017) developed a model based on floc fractal theory that predicts the rheological properties of a wide variety of clays when sheared at different solid-water ratios:

$$\mu_s^{eff} = \left[\tau_0^{\frac{1}{4-D}+\left(1+\frac{1}{\beta\gamma^m}\left(\frac{\tau_0}{\mu_*}\right)^m\right)^{\frac{1}{4-D}}(\mu_*\gamma)^{\frac{1}{4-D}}} \right]^{4-D} \gamma^{-1} \tag{24}$$

$$\tau_0 = \tau^* \left[\frac{\phi_s/\phi_s^{max}}{\left(1-\phi_s/\phi_s^{max}\right)} \right]^{4-D} \quad ; \quad \mu_* = \frac{\mu_f}{\left(1-\phi_s/\phi_s^{max}\right)^2} \tag{25}$$

In equations (24) and (25), ϕ_s^{max} is the maximum solid fraction of clay, τ^* the critical shear stress at $\phi_s = 0.5\,\phi_s^{max}$, D is the fractal dimension, β is a structural parameter, m is a structural break-up parameter, and γ is the strain rate (calculated at each time step as the sum of symmetric components of $\nabla\widehat{U}_s$). With proper tuning, this model was shown to successfully describe the rheologies of smectite, illite, and kaolinite clays. Parameter values were taken from Spearman (2017) based on fitting rheological data pertaining to a 90% smectite-water mixture obtained by Coussot (1993) and are listed in Table 1.

We note that equations (24) and (25) do not explicitly consider potential impacts of salinity or dynamic changes in solid fraction (as in the case of shrinking and swelling) on rheology. Instead, the Spearman model assumes that the clay is at an equilibrated solid fraction when calculating the effective viscosity. For simplicity, we assume that the resulting effective viscosity applies not only to shear, but also to expansion and contraction.

The use of equations (20)–(22), 24, and 25 in the modeling framework derived in section 2 provides closure for the coupled system of equations in the case of pure smectite in sodium electrolytes such as NaCl at salinities up to 0.5 M. As noted above, this closure relies on a number of assumptions and approximations. Notably, it neglects clay fabric anisotropy (Hicher et al., 2017; Tessier, 1990) and clay dispersion into the bulk water phase. Furthermore, it relies on the assumption that DLVO theory, the Kozeny-Carman equation, Spearman's model, and the Fickian diffusion equation described above are accurate in conditions beyond their validation in Figure 3 (for example, during dynamics shearing, shrinking, and swelling). The assumptions and approximations listed above are not intrinsic to the modeling framework derived in section 2. They can be readily addressed in future studies as additional information become available on the microscale permeability, swelling pressure, rheology, and dispersion of microporous clay.

5. Model Validation and Application to Plastically Deformable Porous Media (Clay)

5.1. Model Verification by Comparison to the Fluid-Driven Deformation of a Clay Filter Cake

A quantitative validation of our model was realized by testing its ability to predict the compaction of a clay plug caused by water flow through said plug. To do this, we compared our numerical results to predictions of an analytical model derived by Hewitt et al. (2016) at equivalent experimental conditions. Said analytical model is based on Biot Theory and is able predict the 1-D solid deformation of the plug as a function its initial porosity, the deformation modulus of the solid, and the fluid pressure gradient across the plug. Hewitt et al. (2016) validated their model against experimental results obtained with an elastically deformable microporous medium placed within a 12 cm by 25 cm container based on the assumptions that permeability follows the Kozeny-Carman equation, stresses follow the Terzaghi stress principle, and fluid flow (and thus the resulting deformation-inducing pressure gradient) is governed by Darcy's law.

To replicate these conditions, our simulations where carried out on a 240 by 300 grid representing a 2-D container (12 cm by 15 cm) partially filled with nonswelling clay. We induced fluid flow through the clay by a constant pressure boundary condition at the top of the container, where fluid (and only fluid) was allowed to leave through the lower boundary. In Figure 4, we compare our steady state, nondimentionalized numerical model predictions for Na-smectite against Hewitt's (2016) analytical model at two initial porosity values, showing good agreement between both models. Since Hewitt et al. (2016) did not include a swelling pressure into their analytical framework, we set $p_{swell} = 0$ in our numerical simulations to ensure proper comparison and verification of the flow-deformation mechanics. Please refer to Table 1 for a detailed listing of the parameter used in this and all other subsequent simulations.

The resulting steady state deformation profiles are a result of the balance between the clay's structural forces (critical stress) and the forces imposed by the fluid (viscous drag): As compaction increases, the permeability of the porous medium decreases, which in turn increases the viscous stresses imposed on the medium. At the same time, given a constant pressure gradient, flow through the plug decreases as permeability decreases, which then reduces the magnitude of the viscous stresses. Steady state is achieved once the viscous drag is balanced by the porous medium's structural forces, which explains why systems with a higher initial compaction deform less than their counterparts (Figure 4). The good agreement shown in Figure 4c is expected (both models rely on similar assumptions such as the validity of the Kozeny-Carman equation and Terzaghi

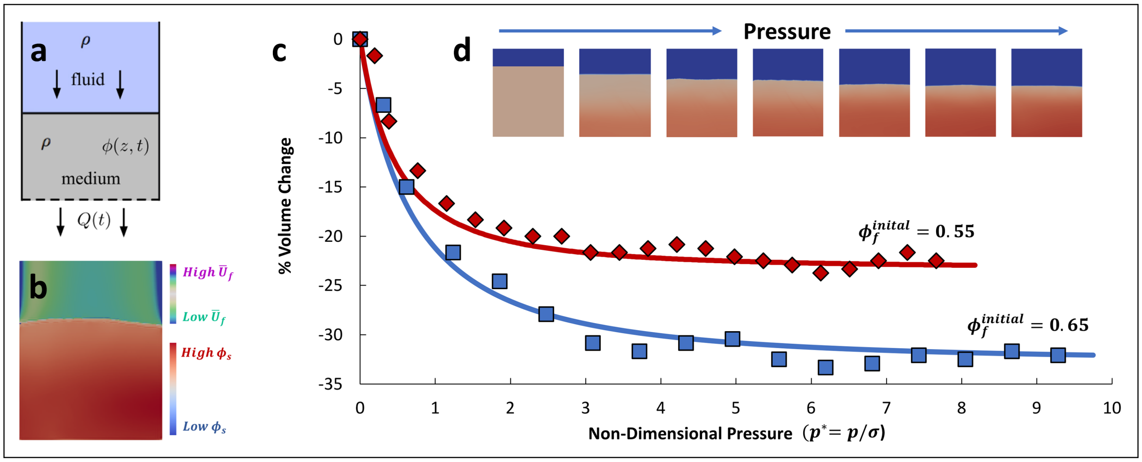

Figure 4. Model prediction of the compaction associated with water flow through a clay plug as a function of pressure drop (from 0 to 200 kPa) across the clay plug: (a) schematic view of the simulated system; (b) equilibrated system as predicted by our simulation framework (colors show clay fraction ϕ_s in the microporous region and fluid velocity $\overline{U}_f$ in the free fluid region); (c) comparison between Hewitt's analytical model (solid lines) and the predictions of our numerical model (symbols) for initial clay porosities of 0.55 and 0.65; and (d) final configurations of the system as a function of increasing pressure drop. The simulations were carried out in a 1 by 300 grid (c) and a 240 by 300 grid (b, d). Results are reported as the nondimensional volume change of the clay plug versus nondimensional pressure drop across the clay plug. Pressure in the simulations was nondimentionalized using a deformation modulus calculated from the clay's critical stress at its initial porosity [$p^* = p/\sigma$, where $\sigma = \tau_0^{initial}/\left(\phi_f^{initial}/\phi_f^{final} - 1\right)$]. For both simulations, mean average error was about 0.04 times the final measured volume change.

and Biot's principles) but also provides some confidence in the ability of our model framework to represent the feedbacks between fluid flow and solid deformation in microporous media.

5.2. Model Verification by Comparison to Oedometric Clay Swelling Experiments

As a further quantitative validation of our model (and to verify the swelling pressure effects disregarded in the previous section), we tested model predictions against standard oedometric measurements of clay swelling driven by a salinity change. Specifically, we used measurements by Di Maio (1996) of the volumetric swelling of water-saturated Na-smectite samples exposed to a salinity shock (from 1 M to 0 M NaCl) at different confining pressures (Figure 5). The experimental conditions were straightforward: individual water-saturated clay samples were first compressed within an oedometer chamber to confining pressures of 40, 160, and 320 kPa. Subsequently, the samples were placed in contact with a 1M NaCl solution through a porous boundary until equilibrated. Swelling was then induced by replacing the saltwater solution with distilled water while maintaining a constant confining pressure.

The swelling portion of the experiments was modeled by defining a 500 by 300 grid representing a 2-D container (5 cm by 3 cm) filled with 2 cm of 1 M NaCl-equilibrated compacted smectite clay, where the clay was only allowed to swell in the positive y direction as a result of salt diffusion out of the container at the lower boundary (where salt concentration was set to zero). All other boundary conditions on the container walls were set to replicate impermeable surfaces with no-slip boundary conditions. For simplicity, the confining pressure was assumed uniform throughout the clay sample and was applied as a constant in the Terzaghi stress tensor (equation (14)).

As shown in Figure 5, our model accurately captures the swelling kinetics of Na-smectite clay driven by osmotic uptake of liquid water. The agreement between our model and experimental data provides further confidence into the ability of our model framework to capture feedbacks between hydrology, mechanics, and salt transport in deformable microporous media. Overall, Figures 4 and 5 show that our model, with no parameter fitting, yields reasonably accurate predictions (with normalized MAEs below 0.09) of the overall extent of clay swelling or compaction and of the associated kinetics. Agreement is obtained regardless of whether the clay volume change is driven by fluid flow (Figure 4) or salinity changes (Figure 5). This good agreement suggests that our model captures key features of the coupled HCM behavior of Na-smectite despite the assumptions and simplifications noted above.

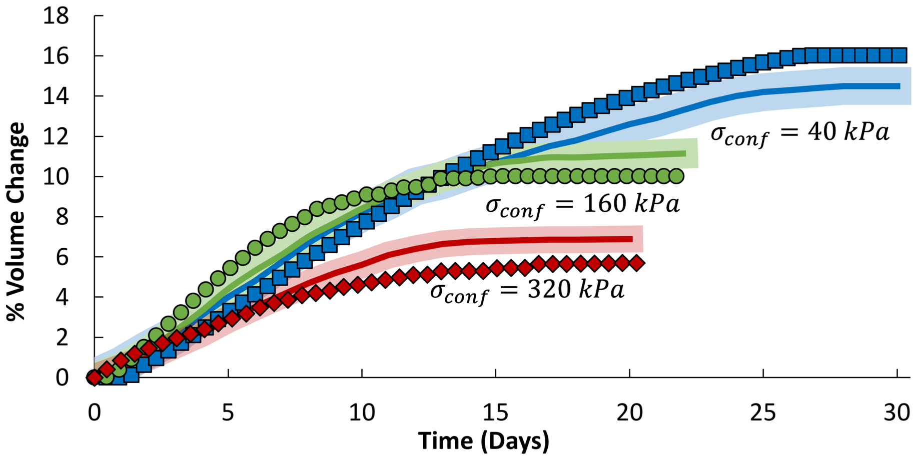

Figure 5. Macroscopic swelling of NaCl-saturated smectite clay (at confining pressures 40, 160, and 320 kPa) initially equilibrated with a 1 M NaCl solution and then placed in contact with a reservoir of distilled water. Experimental results (solid lines) and approximated error (shaded regions) were obtained using data from Di Maio et al. (1996). Simulation predictions (symbols) were obtained using two-dimensional 500 by 300 grids. For the three simulations, mean average error was 0.06 to 0.09 times the measured final volume change.

5.3. Model Prediction of the Permeability of a Bead Pack Containing Na-Smectite as a Function of Salinity and Clay Content

Having parametrized and tested our simulation framework, we used it to predict the permeability of an idealized model of fine-grained soils and sedimentary media: A bead pack containing coarse nonporous beads uniformly coated with Na-smectite clay. The idealized system simulated here has previously been used both as a conceptual model of the hydrology of sedimentary media and as an idealized experimental model of the properties of engineered clay barriers (Abichou et al., 2002; Revil & Cathles, 1999; Tuller & Or, 2003). To the best of our knowledge, it has not been previously implemented in a numerical framework that accounts for the HCM couplings in microporous clay. As implemented here, this model system captures both key features of fine-grained soils and sedimentary media identified in section 1: The coexistence of two characteristic length scales and the HCM coupled properties of the microporous clay. As noted above, Na-smectite is used here because reasonably accurate constitutive models exist to describe its swelling pressure, permeability, and rheology at the microscopic scale, even though the microporous regions in most soil and sedimentary media generally consist of more complex mixtures of Ca/Na-smectite, other clay minerals, and organic matter.

Our simulations are based on a representative, yet simplified, rock geometry built upon the following assumptions: First, the medium's coarse-grained, load-bearing structure can be represented as a 2-D cross-section of a 3-D randomly distributed spherical packed bed with a porosity of 0.64 obtained from Finney (1970); second, the initial distribution of clay is modeled as a uniform film coating the coarse grains (a reasonable approximation given previous imaging studies; Abichou et al., 2002; Aksu et al., 2015; Peters, 2009), and third, a two-dimensional geometry is sufficient to capture major features of the simulated system (as in Quispe et al., 2005). These are significant approximations; in particular, feedbacks between fluid flow and clay dynamics may create some degree of nonuniformity in the clay distribution within sedimentary rocks (Song & Kovscek, 2015) and percolation thresholds associated with pore clogging may occur more readily in two-dimensional than in three-dimensional systems.

The system was simulated as a function of clay mass fraction (from 0 to 0.3) and salinity (from 1 to 1,000 mM NaCl). We chose this parameter space because, as noted in the introduction, it represents the range over which micro and macropores coexist and over which the coarse grains are load bearing. Briefly, we initialized each set of simulations by populating the 3 by 3 mm coarse grain structure with a uniform clay coating equilibrated at 1,000 mM NaCl until we reached the desired clay mass fraction. Clay parametrization was consistent with the verification cases described in the previous sections. We then applied a constant hydrostatic pressure gradient in the *y* direction and a salinity step change across the sample and allowed the clay to swell until it reached its equilibrium volume fraction based on the new salinity value. A representative sample of the resulting steady state configurations as a function of clay mass fraction and salinity is shown in Figure 6. Each sample was put through several swelling-shrinking cycles to ensure consistent results and to introduce heterogeneity approaching that present in natural systems. Although not evident in the equations, heterogeneous clay distributions can arise due to the combination of frictional forces imparted by the solid grains and the clay's non-Newtonian rheology. After we reached the steady state configuration, the permeability of each sample was evaluated by integration of the fluid velocities. Figures illustrating the predicted fluid velocity distribution in a region containing both macropores and microporous clay are shown in Figure 7.

Figure 8a shows that permeability varies by 10 orders of magnitude within the studied parameter space, with the largest permeability reduction (6 orders of magnitude) coming from changing the salinity at clay mass fractions near 15%. This large permeability range reflects the very low permeability of pure Na-smectite and the ability of the clay to block the main preferential fluid flow paths, effectively dividing the medium's macropores into isolated regions. Because of the clay's ability to swell, the location of the percolation threshold depends on both salinity and clay mass fraction.

Further analysis shows that the simulation predictions in Figure 8a collapse into a single relation between $\log(k/k_0)$ and the clay matrix volume fraction V_{clay} (i.e., the ratio of volume occupied by the clay matrix, including its internal microporosity, to the total volume occupied by the clay and coarse grains). As shown in Figure 8b, the main preferential fluid flow path is consistently closed at $V_{\mathrm{clay}} \approx 25\%$ in our simulations, in reasonable agreement with previous predictions for spherical bead packs clogged either by clay or by cementation (Martys et al., 1994; Tuller & Or, 2006). At clay volume fractions below this percolation threshold, clay swelling influences permeability by a relatively small (but still highly significant) 2 orders of magnitude.

To compare the simulation predictions in Figure 8b with experimental data on the permeability of clayey media, we fitted the simulation predictions of $\log(k/k_0)$ versus V_{clay} using an error function:

$$\log\left(\frac{k}{k_0}\right) = \frac{A}{2}\left(\operatorname{erf}\left(S\left(V_{clay} - V^*_{clay}\right)\right) - 1\right) \tag{26}$$

In equation (26), A is the overall magnitude of the decrease in $\log k$, S describes the sensitivity of permeability to V_{clay} near the percolation threshold, and V^*_{clay} describes the location of the threshold. Equation (26) provides a reasonable fit to the simulation predictions in Figure 8b with only three parameters (though it underestimates the sharpness of the threshold). To test the broader validity of equation (26), we identified four experimental data sets that reported the permeability of a series of porous media with similar mineralogy differing only in their clay content and that expressed clay content in the same manner as in Figure 8b (Abichou et al., 2002; Gräfe et al., 2017; Heap et al., 2017; Revil & Cathles, 1999). As shown in Figure 8c, equation (26) provides accurate descriptions of all four data sets. In the five parametric fits carried out with equation (26) in Figures 8b and 8c, the values of S and A were consistently related ($S/A = 1.38 \pm 0.25$). Fitted A values ranged from 4.2 to 9.6, a range consistent with the reported permeability values of different clays, which span 4 to 5 orders of magnitude and increase in the order Na-smectite < Ca-smectite ≈ illite < kaolinite (Mesri & Olson, 1971; Mondol et al., 2008). Fitted values of V^*_{clay} ranged from 0.10 to 0.25, in agreement with the expectation that the location of the percolation threshold depends on the porosity of the network of coarse grains (Aksu et al., 2015), that is, it should be lower for systems with greater cementation or with less uniform grain size distributions. The simulation predictions shown in Figure 8b, as expected, are at the upper end of the range of both A values (because we used the lowest-permeability clay, Na-smectite) and V^*_{clay} values (because we used a 2-D slice of a 3-D bead pack with a uniform bead size and no cementation).

The simulations described in this section are designed to approximate systems where the network of coarse grains is load bearing and where clay influences permeability only through swelling and shrinking in response to salinity changes. Clay erosion, transport, and deposition are not included in our model, while viscous deformation of the clay by the flowing fluid is minimized by the use of a small fluid pressure gradient. Nevertheless, the good agreement between the results obtained with smectite and illite and between the parametric fits to simulated and measured permeabilities suggest that the computational framework used

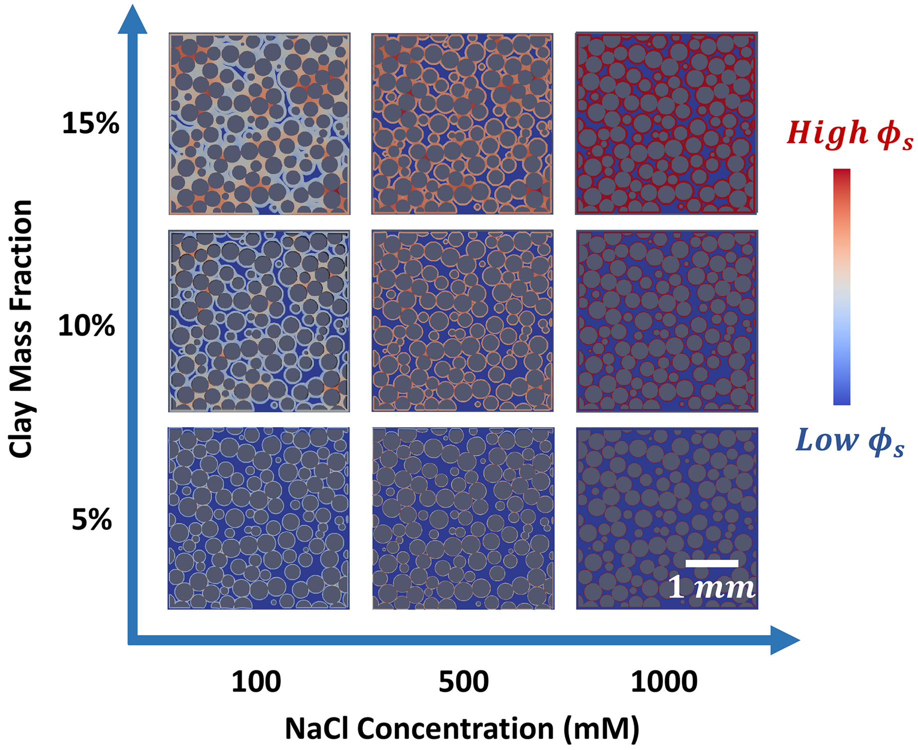

Figure 6. Effect of clay mass fraction and NaCl concentration on the spatial distribution of smectite clay and available macropore space in a 2-D cross section of an ideal 3-D spherical packed bed (Finney, 1970). The simulated system is 3 by 3 mm. The grid resolution is 1020 by 1020 with a voxel size of 3 μm.

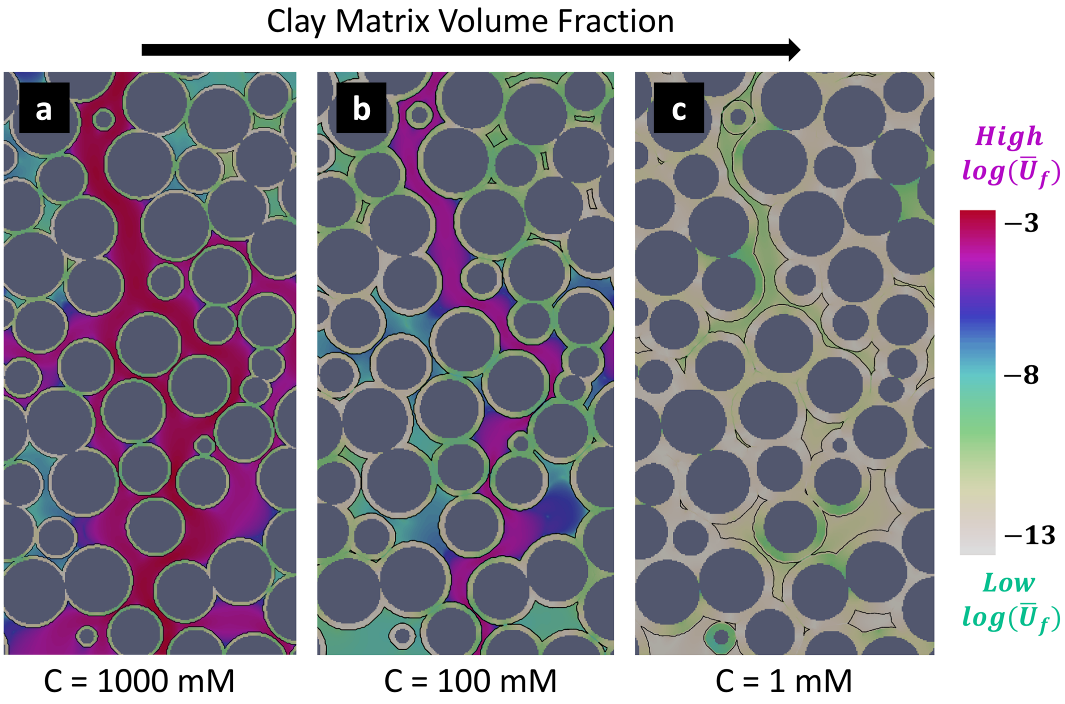

C = 1000 mM C = 100 mM C = 1 mM

Figure 7. Steady state fluid velocity profiles with a 10% clay mass fraction at different salinity values. Thin black lines surrounding the solid grains represent the boundary between the clay matrix (within the lines) and the free fluid (outside the lines). At relatively high salt concentrations (a and b), flow within the clay (greenish shades) does not control the overall permeability of the medium and can be considered negligible when compared to flow around the clay. Conversely, at lower salt concentrations and higher clay volumes (c), flow is controlled by the internal permeability of the clay matrix due to the absence of percolating flow paths through the macropores. The impact on the overall permeability of the system is shown in Figure 8.

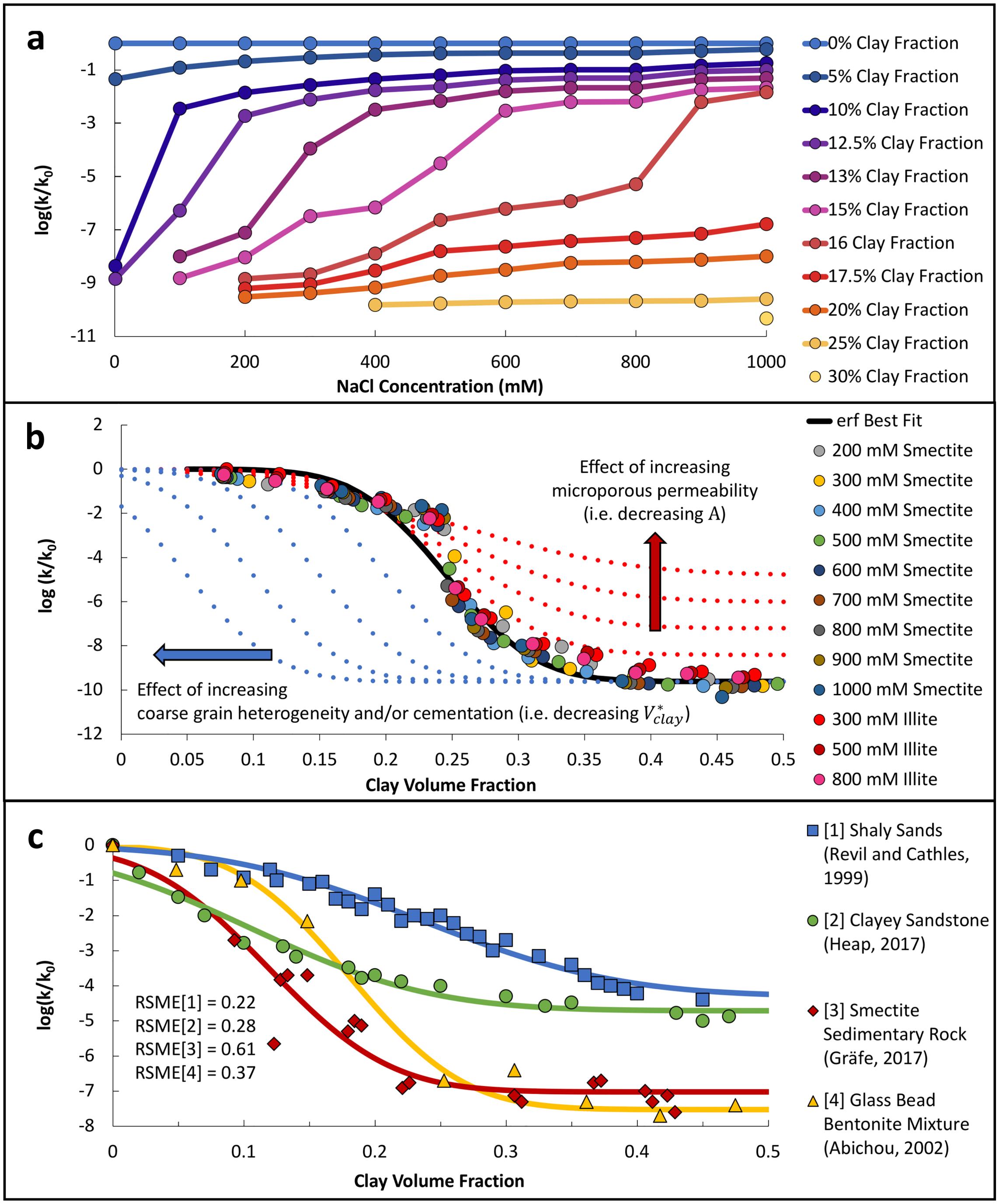

Figure 8. (a) Permeability of the simplified sedimentary rock model in Figure 6 as a function NaCl concentration for a range of smectite clay mass fractions. The unprobed parameter space in the lower left corner represents conditions where clay more than fills the available space between the coarse grains (i.e., clay becomes load bearing). (b) Data from Figure 8a plotted as a function of clay matrix volume fraction. The permeability data collapse into a single curve that can be approximated with an error function (equation (26) with $A = 9.6$, $S = 1.38 \times A$, and $V^*_{clay} = 0.25$). Note that the figure also includes data obtained using equations (20) and (21) parameterized for Illite instead of smectite. The smectite and illite permeabilities coincide below the percolation threshold (where permeability is controlled by flow through macropores) and differ by up to 2 orders of magnitude above the threshold (where flow through the clay matrix predominates). (c) Comparison between equation (26) (solid lines) and experimental data sets on the permeability of three different types of siliciclastic sedimentary rocks (Gräfe et al., 2017; Heap et al., 2017; Revil & Cathles, 1999) and a series of glass bead-smectite mixtures (Abichou et al., 2002). The curves' parameters are: $A_1 = 4.2 \& V^*_{1,clay} = 0.25, A_2 = 4.8 \& V^*_{2,clay} = 0.10, A_3 = 7 \& V^*_{3,clay} = 0.12$, and $A_4 = 7.4 \& V^*_{4,clay} = 0.18$ with $S = 1.38 \times A$.

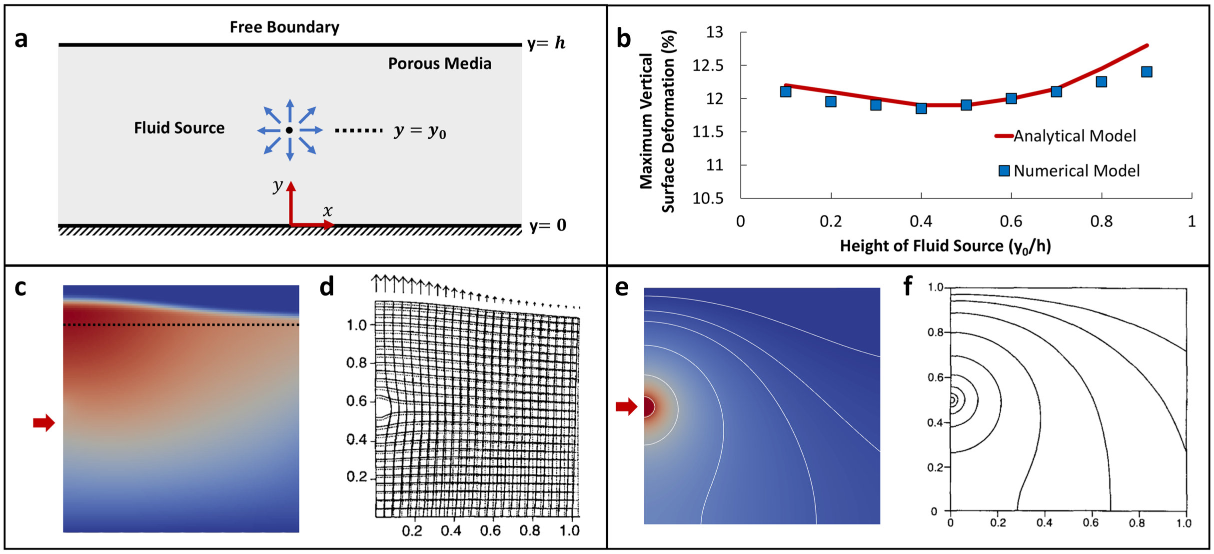

Figure 9. (a) Representation of the modeled system. (b) Quantitative comparison of the maximum vertical deformation as a function of the point fluid source position (y_0/h). Our model correctly predicts the vertical deformation of the material with a mean average error equal to 0.01 times the overall deformation. One potential source of error is the fact that the fluid source in our numerical simulations was fixed in space and did not move upward with solid deformation as it does in the analytical solution. (c–f) Qualitative comparison of the deformation and pressure profiles obtained by our model on a 120 by 150 grid (c and e) and Barry's analytical solution (d and f), respectively. The red arrows in c and e represent the fluid source position in the numerical model. The parameters for these simulations can be found in Table 1.

here may be applicable to clayey media with a range of porosities, clay mineralogies, and configurations. Two additional illustrations of this versatility are included in the SI. The first one shows that the results shown in Figure 8a are qualitatively consistent with measurements of hydraulic conductivity versus salinity in soils (Figure S5). The second one applies this framework to simulate formation damage and chemically driven fracture evolution in fractured rocks (Figure S2).

6. Model Application to Fluid Injection in an Elastically Deformable Porous Medium

As a final illustration of the versatility of the modeling framework developed in section 2, we briefly apply and verify our model for a simple poroelastic system. More precisely, we simulate fluid injection into a symmetric poroelastic material, a model system used to mimic the properties of filters, biological tissues, membranes, and soils (Auton & MacMinn, 2017; Barry et al., 1995; Nagel & Kelly, 2012). Barry et al. (1997) used Biot theory and the assumption that material stress is directly proportional to the fluids' frictional forces (i.e., drag) to obtain an analytical solution for the pressure and deformation profiles brought about by a constant point fluid source placed at different depths in the system shown in Figure 9a. The system studied by Barry (and replicated in our simulations) is defined by a no-slip condition at the lower boundary ($y = 0$), a constant-pressure fluid point source placed at height y_0 on the axis of symmetry ($x = 0$), and zero-gradient boundary conditions at all other boundaries. Please refer to Table 1 and Barry et al. (1997) for the complete parametrization of the simulation.

The complete figure shows that our numerical framework replicates Barry's analytical solutions for the system's maximum deformation in the y direction to a relatively high degree of accuracy for most values of y_0. As stated in the original paper, the minimum at $y_0/h \approx 0.4$ results from two phenomena: First, when the source is near $y/h = 1$, most of the flow leaves through the top boundary, increasing drag near this boundary and maximizing its deformation; second, the maximum vertical deformation is essentially the sum of all local deformations along the axis of symmetry ($x = 0$), meaning that at low values of y_0, fluid drag is able to act over more of the solid, thus increasing the overall accumulated vertical deformation. The sum of these two effects is minimized at intermediate values of y_0, leading to the observed minimum. The tendency of our simulations to underestimate surface deformation at high values of y_0 likely reflects the fact that the location of the fluid source in our simulations is not affected by the solid's deformation, contrary to the analytical solution, a difference most significant at $y_0/h \approx 1$ because of the first phenomenon noted above.

One notable weakness of the simulations presented here is that the fluid-solid interface is not represented as a sharp step function but rather as a continuous interpolation of the stresses between both domains. This loss of sharpness is particularly noticeable as the magnitude of the deformations become large, as seen in Figure 9c, perhaps reflecting the breakdown of the validity of the elastic momentum equation in systems with large deformations. This loss of sharpness is much less apparent in the case of the swelling porous media modeled in the previous section, where the swelling pressure acts in favor of a sharp interface. Errors emanating from the lack of sharpness in elastic porous media could be addressed by the introduction of an artificial compression term (as used in Volume-Of-Fluid models; Rusche, 2002), higher resolution meshes, or the addition a suitable swelling pressure model.

7. Conclusions

We have implemented, tested, and verified a multiscale hydro-chemo-mechanically coupled modeling framework for porous media containing both macropores and deformable microporous regions. This Darcy-Brinkman-Biot framework was derived by volume-averaging the fundamental fluid and solid governing equations, which were then coupled through generic momentum-transfer and effective stress terms derived from Terzaghi, Biot, and Mixture theories. The result is a system of equations that can be parametrized through system-specific rheology, permeability, and swelling pressure models. We demonstrated the framework's accuracy and versatility by modeling HCM-coupled viscoplastic and poroelastic dynamics.

The model was implemented and parametrized in particular to simulate the swelling behavior and fluid-induced deformation of water-saturated viscoplastic Na-smectite clay. Predicted couplings between hydrology, mechanics, and salinity were successfully validated against experimental data and numerical models by Di Maio (1996) and Hewitt et al. (2016) describing a broad range of simulated conditions. The model was then used to predict the permeability of a spherical bead pack as a function of clay content and salinity. For this simple model, a master parametric equation for permeability as a function of clay matrix volume fraction was extracted. This parametric equation was found to be consistent with experimental data sets on the permeability of smectite-coated glass bead packs and of different types of siliciclastic sedimentary rocks. Finally, the model's versatility was demonstrated by qualitatively predicting water-induced formation damage in a propped fracture in clayey rock and, also, by quantitatively predicting the pressure fields and deformation profiles resulting from fluid injection in an elastically deformable axisymmetric porous medium, for which analytical solutions were developed by Barry et al. (1997).

Although the proposed framework has proven relatively accurate in the conditions examined, it comes with several limitations, many of which can be addressed in the future: (a) Closure of the system of equations requires appropriate constitutive relations describing the sub-REV-scale swelling pressure, permeability, and rheology of the microporous regions; in the case of clayey media, knowledge of these relations is required in a broader range of clay mineralogy, porosity, and aqueous chemistry conditions; (b) the model can only be used for systems where the size of the macropores is substantially larger than that of the micropores, because of the length-scale separation condition required during volume-averaging; (c) the proposed framework cannot describe systems where the microporous medium exhibits fluidization and is restricted to continuum-level mechanics where the microporous medium behaves as either a plastic or an elastic solid; (d) the fluid behavior at the fluid-microporous interface is an approximation that originates from the continuous interpolation of fluid and solid flow properties, meaning that the framework cannot be used in instances where a rigorous tracking of interface dynamics is required; (e) the system only works for single-fluid saturated systems, a limitation that makes the introduction of multi-phase flow the next logical step in the further development of this model; finally, (f) the model is a continuum level simulation; therefore, it cannot capture behaviors originating from microstructure heterogeneity such as the coexistence of different pore sizes within the microporous clay.

We have demonstrated the limitations, flexibility, accuracy, and usefulness of a novel modeling framework for the simulation of multiscale hydro-chemo-mechanically coupled deformable porous media. Future work involves the addition of multiphase flow, heat transfer, porous media ionic exclusion models, dissolution/precipitation dynamics, and reactive-transport models.

Acknowledgments

This research was supported equally by the U.S. Department of Energy, Office of Science, Office of Basic Energy Sciences (DOE-BES) EFRC program under award DE-AC02-05CH11231 (through the Center for Nanoscale Controls on Geologic CO_2) and by the National Science Foundation Division of Earth Sciences (NSF EAR) CAREER program under award EAR-1752982. We thank the Princeton Institute for Computational Science and Engineering for computational support, Howard Stone (Princeton University) for his insightful comments, Cyprien Soulaine (French Geological Survey) for productive discussions, and our reviewers and editors, all of whom greatly increased the quality of this manuscript. We do not report any conflicts of interest. A full compilation of the data used in this manuscript can be found under DOI:10.17632/xfx7734xvv.2 (Carrillo & Bourg, 2019).

References

Abichou, T., Benson, C. H., & Edil, T. B. (2002). Micro-structure and hydraulic conductivity of simulated sand-bentonite mixtures. *Clays and Clay Minerals*, *50*(5), 537–545. https://doi.org/10.1346/000986002320679422

Adair, J. H., Suvaci, E., & Sindel, J. (2001). *Surface and colloid chemistry. Encyclopedia of Materials: Science and Technology*. Amsterdam, Netherlands: Elsevier. doi: https://doi.org/10.1016/B0-08-043152-6/01622-3

Adler, P. M., Jacquin, C. G., & Thovert, J. F. (1992). The formation factor of reconstructed porous media. *Water Resources Research*, *28*(6), 1571–1576. https://doi.org/10.1029/92WR00059

Aksu, I., Bazilevskaya, E., & Karpyn, Z. T. (2015). Swelling of clay minerals in unconsolidated porous media and its impact on permeability. *Geographical Research Journal*, *7*, 1–13. https://doi.org/10.1016/j.grj.2015.02.003

Alvarado, V., & Manrique, E. (2010). Enhanced oil recovery: An update review. *Energies*, *3*(9), 1529–1575. https://doi.org/10.3390/en3091529

Auton, L. C., & MacMinn, C. W. (2017). From arteries to boreholes: Steady-state response of a poroelastic cylinder to fluid injection. *Proceedings of the Royal Society A: Mathematical, Physical and Engineering Science*, *473*(2201), 20160753). https://doi.org/10.1098/rspa.2016.0753

Badia, S., Quaini, A., & Quarteroni, A. (2009). Coupling Biot and Navier-Stokes equations for modelling fluid-poroelastic media interaction. *Journal of Computational Physics*, *228*(21), 7986–8014. https://doi.org/10.1016/j.jcp.2009.07.019

Barbier, E. (1997). Nature and technology of geothermal energy: A review. *Renewable and Sustainable Energy Reviews* Retrieved from https://pdf.sciencedirectassets.com/271969/1-s2.0-S1364032100X0038X/1-s2.0-S1364032197000014/main.pdf?x-amz-security-token=AgoJb3JpZ2luX2VjEPD%2F%2F%2F%2F%2F%2F%2F%2F%2F%2FwEaCXVzLWVhc3QtMSJIMEYCIQC7qiRO9ppghlNm6CpQ4O72SM3cj12J21J6fXO6AnZ92QIhALxAWZZqZyIz, (1-2), –69. https://doi.org/10.1016/S1364-0321(97)00001-4

Barry, S., Aldis, G., & Mercer, G. (1995). Injection of fluid into a layer of deformable porous medium. *Applied Mechanics Reviews*, *48*(10), 722. https://doi.org/10.1115/1.3005054

Barry, S. I., & Aldis, G. K. (1992). Flow-induced deformation from pressurized cavities in absorbing porous tissues. *Bulletin of Mathematical Biology*, *54*(6), 977–997. Retrieved from https://ac.els-cdn.com/S0092824005800916/1-s2.0-S0092824005800916-main.pdf?_tid=9a63039f-b67d-4e28-a0e5-a7a53e338014&acdnat=1521489449_0451b532cbe571b44c2603e39278d388, https://doi.org/10.1007/BF02460662

Barry, S. I., Mercer, G. N., & Zoppou, C. (1997). Deformation and fluid flow due to a source in a poro-elastic layer. *Applied Mathematical Modelling*, *21*(11), 681–689. https://doi.org/10.1016/S0307-904X(97)00097-8

Batty, C., Bertails, F., & Bridson, R. (2007). A fast variational framework for accurate solid-fluid coupling. *ACM Transactions on Graphics*, *26*(3), 100. https://doi.org/10.1145/1276377.1276502

Beavers, G. S., & Joseph, D. D. (1967). Boundary conditions at a naturally permeable wall. *Journal of Fluid Mechanics*, *30*(1), 197–207. https://doi.org/10.1017/S0022112067001375

Berg, R. (1970). Method for determining permeability from reservoir rock properties. In *Transactions - Gulf Coast Association of Geological Societies*. Houston, TX: Gulf Coast Association of Geological Societies Transactions, 303 –317. Retrieved from http://archives.datapages.com/data/gcags/data/020/020001/pdfs/0303.pdf

Bertrand, T., Peixinho, J., Mukhopadhyay, S., & MacMinn, C. W. (2016). Dynamics of swelling and drying in a spherical gel. *Physical Review Applied*, *6*(6), 064010. https://doi.org/10.1103/PhysRevApplied.6.064010

Bijeljic, B., Raeini, A. Q., Lin, Q., & Blunt, M. J. (2018). Multimodal Functions as Flow Signatures in Complex Porous Media. Retrieved from http://arxiv.org/abs/1807.07611

Biot, M. A. (1941). General theory of three-dimensional consolidation. *Journal of Applied Physics*, *12*(2), 155–164. https://doi.org/10.1063/1.1712886

Blum, P., Scheunemann, M., Van Loon, L., Coelho, D., Maes, N., & Grathwohl, P. (2007). Evaluating the application of Archie's Law for argillaceous rocks. In *Clays in Natural & Engineered Barriers for Radioactive Waste Confinement*, (pp. 483–484). Lille, France: Andra. Retrieved from http://www.andra.fr/mini-sites/lille2007/abstract_lille2007/donnees/pdf/483_484_P_MTPM_31.pdf

Bourg, I. C. (2015). Sealing shales versus brittle shales: A sharp threshold in the material properties and energy technology uses of fine-grained sedimentary rocks. *Environmental Science & Technology Letters*, *2*(10), 255–259. https://doi.org/10.1021/acs.estlett.5b00233

Bourg, I. C., & Ajo-Franklin, J. B. (2017). Clay, Water, and Salt: Controls on the permeability of fine-grained sedimentary rocks. *Accounts of Chemical Research*, *50*(9), 2067–2074. https://doi.org/10.1021/acs.accounts.7b00261

Bourg, I. C., Sposito, G., & Bourg, A. C. M. (2006). Tracer diffusion in compacted, water-saturated bentonite. *Clays and Clay Minerals*, *54*(3), 363–374. https://doi.org/10.1346/CCMN.2006.0540307

Boving, T. B., & Grathwohl, P. (2001). Tracer diffusion coefficients in sedimentary rocks: Correlation to porosity and hydraulic conductivity. *Journal of Contaminant Hydrology*, *53*(1–2), 85–100. https://doi.org/10.1016/S0169-7722(01)00138-3

Brace, W. F. (1980). Permeability of crystalline and argillaceous rocks. *International Journal of Rock Mechanics and Mining Sciences and Geomechanics*, *17*(5), 241–251. https://doi.org/10.1016/0148-9062(80)90807-4

Breugmem, W.-P., & Verzicco, R. (2013). Immersed boundary methods: Current status and future research directions. In *Euromech Colloquium 549* (Chap. 1, pp. 37–45). Amsterdam: The Royal Netherlands Academy of Arts and Sciences. https://doi.org/978-90-6984-590-6

Brinkman, H. C. (1947). A calculation of the viscous force exerted by a flowing fluid on a dense swarm of particles. *Applied Scientific Research*, *2*(1), 155–161. https://doi.org/10.1007/BF00411979

Brooks, C. (1955). Nitrogen adsorption experiments on several clay minerals. *Soil Science*, *79*(5), 331–348. Retrieved from http://journals.lww.com/soilsci/Abstract/1955/05000/Nitrogen_Adsorption_Experiments_on_Several_Clay.2.aspx. https://doi.org/10.1097/00010694-195505000-00002

Carey, J. W., Mori, H., Brown, D., & Pawar, R. (2014). Geomechanical behavior of caprock and cement: Plasticity in hydrodynamic seals. *Energy Procedia*, *63*, 5671–5679. https://doi.org/10.1016/j.egypro.2014.11.600

Carrillo, F. J., & Bourg, I. C. (2019). A Darcy-Brinkman-Biot approach to modeling the hydrology and mechanics of porous media containing macropores and deformable microporous regions data. *Mendeley Data Repository*, *2*, 1–13. https://doi.org/10.17632/XFX7734XVV.2

Chapuis, R. P., & Aubertin, M. (2003). Predicting the coefficient permeability of soils using the Kozeny-Carman equation. *École Polytechnique de Montréal*, (January), 1–31. Retrieved from http://www.polymtl.ca/biblio/epmrt/rapports/rt2003-03.pdf

Coussot, P., Leonov, A. I., & Piau, J. M. (1993). Rheology of concentrated dispersed systems in a low molecular weight matrix. *Journal of Non-Newtonian Fluid Mechanics*, *46*(2-3), 179–217. https://doi.org/10.1016/0377-0257(93)85046-d

Crawford, B. R., Faulkner, D. R., & Rutter, E. H. (2008). Strength, porosity, and permeability development during hydrostatic and shear loading of synthetic quartz-clay fault gouge. *Journal of Geophysical Research*, *113*, 1, B03207–14. https://doi.org/10.1029/2006JB004634

Crowe, C. T., Schwarzkopf, J. D., Sommerfeld, M., & Tsuji, Y. (2011). Multiphase FLOW WITH DROPLETS AND PARTICLEs. *CRC Press Taylor & Francis Group*, 209.

Dai, Z., Peng, Y., Henry, B. M., Mansy, H. A., Sandler, R. H., & Royston, T. J. (2014). A comprehensive computational model of sound transmission through the porcine lung. *The Journal of the Acoustical Society of America*, *136*(3), 1419–1429. https://doi.org/10.1121/1.4890647

Datta, S. S., Preska Steinberg, A., & Ismagilov, R. F. (2016). Polymers in the gut compress the colonic mucus hydrogel. *Proceedings of the National Academy of Sciences*, *113*(26), 7041–7046. https://doi.org/10.1073/pnas.1602789113

Di Maio, C. (1996). Exposure of bentonite to salt solution: osmotic and mechanical effects. *Géotechnique*, *46*(4), 695–707. https://doi.org/10.1680/geot.1996.46.4.695

Diamond, S., & Kinter, E. B. (1956). Surface areas of clay minerals as derived from measurements of glycerol retention. *Clays and Clay Minerals*, *5*(1), 334–347. https://doi.org/10.1346/CCMN.1956.0050128

Dixon, D. A., Graham, J., & Gray, M. N. (1999). Hydraulic conductivity of clays in confined tests under low hydraulic gradients. *Canadian Geotechnical Journal*, *36*(5), 815–825. https://doi.org/10.1139/t99-057

Ehrhardt, M. (2010). an introduction to fluid-porous interface coupling. *Progress in Computational Physics*, *2*, 3–12. https://doi.org/10.2174/978160805254711202010003

Erol, O. (1977). *Clay structure and creep behavior of clays as a rate process*. Ames, Iowa, United States: Iowa State University. Retrieved from http://lib.dr.iastate.edu/rtd

Fiès, J. C., & Bruand, A. (1998). Particle packing and organization of the textural porosity in clay-silt-sand mixtures. *European Journal of Soil Science*, *49*(4), 557–567. https://doi.org/10.1046/j.1365-2389.1998.4940557.x

Finney, J. L. (1970). Random packings and the structure of simple liquids. I. The geometry of random close packing. *Proceedings of the Royal Society A: Mathematical, Physical and Engineering Sciences*, *319*(1539), 479–493. https://doi.org/10.1098/rspa.1970.0189

Fredrich, J. T. (1999). 3D imaging of porous media using laser scanning confocal microscopy with application to microscale transport processes. *Physics and Chemistry of the Earth, Part A: Solid Earth and Geodesy*, *24*(7), 551–561. https://doi.org/10.1016/S1464-1895(99)00079-4

Gilbert, B., Comolli, L. R., Tinnacher, R. M., Kunz, M., & Banfield, J. F. (2015). Formation and restacking of disordered smectite osmotic hydrates. *Clays and Clay Minerals*, *63*(6), 432–442. https://doi.org/10.1346/CCMN.2015.0630602

Golfier, F., Lasseux, D., & Quintard, M. (2015). Investigation of the effective permeability of vuggy or fractured porous media from a Darcy-Brinkman approach. *Computational Geosciences*, *19*(1), 63–78. https://doi.org/10.1007/s10596-014-9448-5

Gräfe, M., Klauber, C., McFarlane, A. J., & Robinson, D. J. (2017). *Clays in the minerals processing value chain. Clays in the Minerals Processing Value Chain*. Cambridge, UK: Cambridge University Press. doi: https://doi.org/10.1017/9781316661888

Guo, B., Ma, L., & Tchelepi, H. A. (2018). Image-based micro-continuum model for gas flow in organic-rich shale rock. *Advances in Water Resources*, *122*, 70–84. https://doi.org/10.1016/j.advwatres.2018.10.004

Güven, N. (1993). Rheological aspects of aqueous smectite suspensions. In *Clay Water Interface and Its Rheological Implications* (Vol. 4, pp. 1–79). Texas Tech University: Lubbock, Texas.

Hamaker, H. C. (1937). The London-van der Waals attraction between spherical particles. *Physica*, *4*(10), 1058–1072. https://doi.org/10.1016/S0031-8914(37)80203-7

Hassanizadeh, M., & Gray, W. G. (1979). General conservation equations for multi-phase systems: 1. Averaging procedure. *Advances in Water Resources*, *2*(C), 131–144. https://doi.org/10.1016/0309-1708(79)90025-3

Hassanizadeh, S. M. (1986). Derivation of basic equation of mass transport in porous media, Part 1. Macroscopic balance laws. *Advances in Water Resources*, *9*(4), 196–206. https://doi.org/10.1016/0309-1708(86)90024-2

Heap, M. J., Kushnir, A. R. L., Gilg, H. A., Wadsworth, F. B., Reuschlé, T., & Baud, P. (2017). Microstructural and petrophysical properties of the Permo-Triassic sandstones (Buntsandstein) from the Soultz-sous-Forêts geothermal site (France). *Geothermal Energy*, *5*(1), 26. https://doi.org/10.1186/s40517-017-0085-9

Hewitt, D. R., Nijjer, J. S., Worster, M. G., & Neufeld, J. A. (2016). Flow-induced compaction of a deformable porous medium. *Physical Review E*, *93*(2). https://doi.org/10.1103/PhysRevE.93.023116

Hicher, P. Y., Wayudi, H., Tessier, D., Hicher, P. Y., Wayudi, H., & Tessier, D. (2017). Microstructural analysis of inherent and induced anisotropy in clay. *Mechanics of Cohesive-frictional Materials*, *5*(5), 341–371. https://doi.org/10.1002/1099-1484(200007)5:53.0.CO;2-C

Holtzman, R., & Juanes, R. (2010). Crossover from fingering to fracturing in deformable disordered media. *Physical Review E - Statistical, Nonlinear, and Soft Matter Physics*, *82*(4), 046305. https://doi.org/10.1103/PhysRevE.82.046305

Hsu, C. T., & Cheng, P. (1990). Thermal dispersion in a porous medium. *International Journal of Heat and Mass Transfer*, *33*(8), 1587–1597. https://doi.org/10.1016/0017-9310(90)90015-M

Jain, A. K., & Juanes, R. (2009). Preferential mode of gas invasion in sediments: Grain-scale mechanistic model of coupled multiphase fluid flow and sediment mechanics. *Journal of Geophysical Research*, *114*, 1–19. https://doi.org/10.1029/2008JB006002

Jasak, H., & Weller, H. G. (2000). Application of the finite volume method and unstructured meshes to linear elasticity. *International Journal for Numerical Methods in Engineering*, *48*(2), 267–287. https://doi.org/10.1002/(SICI)1097-0207(20000520)48:2<267:AID-NME884>3.0.CO;2-Q, https://doi.org/10.1002/(SICI)1097-0207(20000520)48:2<267::AID-NME884>3.0.CO;2-Q

Karnland, O., Olsson, S., Nilsson, U., & Sellin, P. (2007). Experimentally determined swelling pressures and geochemical interactions of compacted Wyoming bentonite with highly alkaline solutions. *Physics and Chemistry of the Earth*, *32*(1–7), 275–286. https://doi.org/10.1016/j.pce.2006.01.012

Keller, L. M., Schuetz, P., Erni, R., Rossell, M. D., Lucas, F., Gasser, P., & Holzer, L. (2013). Characterization of multi-scale microstructural features in Opalinus Clay. *Microporous and Mesoporous Materials*, *170*, 83–94. https://doi.org/10.1016/j.micromeso.2012.11.029

Kemper, W. D., & Quirk, J. P. (1972). Ion mobilities and electric charge of external clay surfaces inferred from potential differences and osmotic flow. *Division S-2 Soil Chemistry*, *36*, 426–433.

Kemper, W. D., & Rollins, J. B. (1966). Osmotic efficiency coefficients across compacted clays 1. *Soil Science Society of America Journal*, *30*(5), 529. https://doi.org/10.2136/sssaj1966.03615995003000050005x

Kemper, W. D., & van Schaik, J. C. (1966). Diffusion of salts in clay-water systems. *Soil Science Society of America Journal*, *30*(5), 534. https://doi.org/10.2136/sssaj1966.03615995003000050006x

Klaus, S. (2003). A guide to CO_2 sequestration. *Science*, *300*(5626), 1677–1682.

Kwon, O., Herbert, B. E., & Kronenberg, A. K. (2004). Permeability of illite-bearing shale: 2. Influence of fluid chemistry on flow and functionally connected pores. *Journal of Geophysical Research B*, *109*(B10), 1–13. https://doi.org/10.1029/2004JB003055

Langmuir, I. (1938). Repulsive forces between charged surfaces in water, and the cause of the Jones-Ray effect. *Science*, *88*(2288), 430–432. https://doi.org/10.1126/science.88.2288.430

Lin, Q., Al-Khulaifi, Y., Blunt, M. J., & Bijeljic, B. (2016). Quantification of sub-resolution porosity in carbonate rocks by applying high-salinity contrast brine using X-ray microtomography differential imaging. *Advances in Water Resources*, *96*, 306–322. https://doi.org/10.1016/j.advwatres.2016.08.002

Liu, L. (2013). Prediction of swelling pressures of different types of bentonite in dilute solutions. *Colloids and Surfaces A: Physicochemical and Engineering Aspects*, *434*, 303–318. https://doi.org/10.1016/j.colsurfa.2013.05.068

Liu, L., & Neretnieks, I. (2008). Homo-interaction between parallel plates at constant charge. *Colloids and Surfaces A: Physicochemical and Engineering Aspects*, *317*(1–3), 636–642. https://doi.org/10.1016/j.colsurfa.2007.11.055

Maciel, G. D. F., Dos Santos, H. K., & Ferreira, F. D. O. (2009). Rheological analysis of water clay compositions in order to investigate mudflows developing in canals. *Journal of the Brazilian Society of Mechanical Sciences and Engineering*, *31*(1), 64–74. https://doi.org/10.1590/S1678-58782009000100010

Madsen, F. T., & Muller-Vonmoos, M. (1989). The swelling behaviour of clays. *Applied Clay Science Elsevier Science Publishers B. V*, *4*, 143–156. Retrieved from https://ac.els-cdn.com/0169131789900057/1-s2.0-0169131789900057-main.pdf?_tid=c4ca342e-0a8d-11e8-afee-00000aab0f6c&acdnat=1517846653_289a4300087fccdbf6929d526d0f48af

Malek, K., & Coppens, M. O. (2003). Knudsen self- and Fickian diffusion in rough nanoporous media. *Journal of Chemical Physics*, *119*(5), 2801–2811. https://doi.org/10.1063/1.1584652

Malusis, M. A., Shackelford, C. D., & Olsen, H. W. (2003). Flow and transport through clay membrane barriers. *Engineering Geology*, *70*(3–4), 235–248. https://doi.org/10.1016/S0013-7952(03)00092-9

Marion, D., Nur, A., Yin, H., & Han, D. (1992). Compressional velocity and porosity in sand-clay mixtures. *Geophysics*, *57*(4), 554–563. https://doi.org/10.1190/1.1443269

Martys, N. S., Torquato, S., & Bentz, D. P. (1994). Universal scaling of fluid permeability for sphere packings. *Physical Review E*, *50*(1), 403–408. https://doi.org/10.1103/physreve.50.403

McBride, M. B. (1997). A critique of diffuse double layer models applied to colloid and surface chemistry. *Clays and Clay Minerals*, *45*(4), 598–608. https://doi.org/10.1346/CCMN.1997.0450412

Mehmani, A., & Prodanović, M. (2011). The effect of microporosity on transport properties in tight reservoirs. *SPE North American Unconventional Gas Conference and Exhibition Held in The Woodlands, Texas, USA, 14–16 June 2011. This*, *63*, 104–119. https://doi.org/10.1016/j.advwatres.2013.10.009

Mehmani, A., & Prodanović, M. (2014). The effect of microporosity on transport properties in porous media. *Advances in Water Resources*, *63*, 104–119. https://doi.org/10.1016/j.advwatres.2013.10.009

Mehmani, A., Prodanović, M., & Javadpour, F. (2013). Multiscale, multiphysics network modeling of shale matrix gas flows. *Transport in Porous Media*, *99*(2), 377–390. https://doi.org/10.1007/s11242-013-0191-5

Mesri, G., & Olson, R. E. (1971). Mechanisms controlling the permeability of clays. *Clays and Clay Minerals*, *19*(3), 151–158. https://doi.org/10.1346/CCMN.1971.0190303

Metz, B., Davidson, O., de Coninck, H., Loos, M., & Meyer, L. (2005). *Carbon dioxide capture and storage. IPCC Special Report*, (1st ed., Vol. 33). New York: Cambridge University Press.

Mirabolghasemi, M., Prodanovic, M., DiCarlo, D., & Ji, H. (2015). Prediction of empirical properties using direct pore-scale simulation of straining through 3D microtomography images of porous media. *Journal of Hydrology*, *529*(P3), 768–778. https://doi.org/10.1016/j.jhydrol.2015.08.016

Missana, T., & Adell, A. (2000). On the applicability of DLVO theory to the prediction of clay colloids stability. *Journal of Colloid and Interface Science*, *230*(1), 150–156. https://doi.org/10.1006/jcis.2000.7003

Mondol, N. H., Bjorlykke, K., & Jahren, J. (2008). Experimental compaction of clays: Relationship between permeability and petrophysical properties in mudstones. *Petroleum Geoscience*, *14*(4), 319–337. https://doi.org/10.1144/1354-079308-773

Mungan, N. (1965). Permeability reduction through changes in pH and salinity. *Journal of Petroleum Technology*, *17*(12), 1449–1453. https://doi.org/10.2118/1283-PA

Murad, M. A., & Cushman, J. H. (1996). Multiscale flow and deformation in hydrophilic swelling porous media. *International Journal of Engineering Science*, *34*(3), 313–338. https://doi.org/10.1016/0020-7225(95)00057-7

Murad, M. a., & Cushman, J. H. (1997). A multiscale theory of swelling porous media: II. Dual porosity models for consolidation of clays incorporating physicochemical effects. *Transport in Porous Media*, *28*(1), 69–108. https://doi.org/10.1023/A:1006539928751

Nadeau, P. H. (1998). An experimental study of the effects of diagenetic clay minerals on reservoir sands. *Clays and Clay Minerals*, *46*(1), 18–26. https://doi.org/10.1346/CCMN.1998.0460103

Nadeev, A., Mikhailov, D., Chuvilin, E., Koroteev, D., & Shako, V. (2013). Visualization of clay and frozen substances inside porous rocks using X-ray micro-computed tomography. *Microscopy and Analysis*, *27*(March), 8–10. Retrieved from http://www.microscopy-analysis.com/sites/default/files/2013_March_Nadeev.pdf

Nagel, T., & Kelly, D. J. (2012). Mechanically induced structural changes during dynamic compression of engineered cartilaginous constructs can potentially explain increases in bulk mechanical properties. *Journal of the Royal Society Interface*, *9*(69), 777–789. https://doi.org/10.1098/rsif.2011.0449

Neale, G., & Nader, W. (1974). Practical significance of Brinkman's extension of Darcy's law: Coupled parallel flows within a channel and a bounding porous medium. *The Canadian Journal of Chemical Engineering*, *52*(4), 475–478. https://doi.org/10.1002/cjce.5450520407

Nelson, P. (1994). Permeability-porosity relationships in sedimentary rocks. *The Log Analyst.*, *56*, 33–40. https://doi.org/10.1016/j.compbiolchem.2015.02.018

Neuzil, C. E. (2013). Can shale safely Host U.S. nuclear waste? *Eos, Transactions American Geophysical Union*, *94*(30), 261–262. https://doi.org/10.1002/2013EO300001

Nield, D. A. (2009). The Beavers–Joseph boundary condition and related matters: A historical and critical note. *Transport in Porous Media*, *78*(3), 537–540. https://doi.org/10.1007/s11242-009-9344-y

Noiriel, C., Madé, B., & Gouze, P. (2007). Impact of coating development on the hydraulic and transport properties in argillaceous limestone fracture. *Water Resources Research*, *43*, W09406. https://doi.org/10.1029/2006WR005379

Nole, M., Daigle, H., Milliken, K. L., & Prodanovic, M. (2016). A method for estimating microporosity of fine-grained sediments and sedimentary rocks via scanning electron microscope image analysis. *Sedimentology*, *63*(6), 1507–1521. https://doi.org/10.1111/sed.12271

Norrish, K. (1954). The swelling of montmorillonite. *Discussions of the Faraday Society*, *18*, 120–134. Retrieved from http://pubs.rsc.org/en/Content/ArticlePDF/1954/DF/DF9541800120. https://doi.org/10.1039/df9541800120

Ochoa-Tapia, J. A., & Whitaker, S. (1995). Momentum transfer at the boundary between a porous medium and a homogeneous fluid-I. Theoretical development. *International Journal of Heat and Mass Transfer*, *38*(14), 2635–2646. https://doi.org/10.1016/0017-9310(94)00346-W

Orchiston, H. D. (1954). Adsorption of water vapor: II. Clays at 25°c. *Soil Science*, *78*(6), 463–480. https://doi.org/10.1097/00010694-195412000-00006

Pashley, R. M., & Israelachvili, J. N. (1984). DLVO and hydration forces between mica surfaces in Mg2+, Ca 2+, Sr 2+, and Ba 2+ chloride solutions. *Journal of Colloid and Interface Science*, *97*(2), 446–455. Retrieved from https://ac.els-cdn.com/0021979784903163/1-s2.0-0021979784903163-main.pdf?_tid=29549a81-3855-4892-8ff8-65ef948ebe11&acdnat=1534187535_f72e43209934ad3f26263b8aeb45a907, https://doi.org/10.1016/0021-9797(84)90316-3

Peters, C. A. (2009). Accessibilities of reactive minerals in consolidated sedimentary rock: An imaging study of three sandstones. *Chemical Geology*, *265*(1–2), 198–208. https://doi.org/10.1016/j.chemgeo.2008.11.014

Pijaudier-Cabot, G., Vermorel, R., Miqueu, C., & Mendiboure, B. (2011). Revisiting poromechanics in the context of microporous materials. *Comptes Rendus Mecanique*, *339*(12), 770–778. https://doi.org/10.1016/j.crme.2011.09.003

Prevost, J.-H. (1978). Anisotropic undrained stress-strain behavior of clays. *Journal of Geotechnical and Geoenvironmental*, *104*(8), 1075–1090. Retrieved from http://trid.trb.org/view.aspx?id=80706

Prodanović, M., Mehmani, A., & Sheppard, A. P. (2015). Imaged-based multiscale network modelling of microporosity in carbonates. *Geological Society, London, Special Publications*, *406*(1), 95–113. https://doi.org/10.1144/SP406.9

Quirk, J. P. (1955). Significance of surface areas calculated from water vapor sorption isotherms by use of the B.E.T. Equation. *Soil Science*, *80*(6), 423–430. https://doi.org/10.1097/00010694-195512000-00001

Quirk, J. P. (1986). Soil permeability in relation to sodicity and salinity. *Philosophical Transactions of the Royal Society of London, Series A: Mathematical, Physical and Engineering Sciences*, *316*(1537), 297–317. https://doi.org/10.1098/rsta.1986.0010

Quispe, J. R., Rozas, R. E., & Toledo, P. G. (2005). Permeability–porosity relationship from a geometrical model of shrinking and lattice Boltzmann and Monte Carlo simulations of flow in two-dimensional pore networks. *Chemical Engineering Journal*, *111*(2-3), 225-236. https://doi.org/10.1016/j.cej.2005.02.003

Raeini, A. Q., Bijeljic, B., & Blunt, M. J. (2017). Generalized network modeling: Network extraction as a coarse-scale discretization of the void space of porous media. *Physical Review E*, *96*(1), 1–17. https://doi.org/10.1103/PhysRevE.96.013312

Ren, X., Zhao, Y., Deng, Q., Kang, J., Li, D., & Wang, D. (2016). A relation of hydraulic conductivity—Void ratio for soils based on Kozeny-Carman equation. *Engineering Geology*, *213*, 89–97. https://doi.org/10.1016/j.enggeo.2016.08.017

Revil, A., & Cathles, L. M. (1999). Permeability of shaly sands. *Water Resources Research*, *35*(3), 651–662. https://doi.org/10.1029/98WR02700

Revil, A., Woodruff, W. F., & Lu, N. (2011). Constitutive equations for coupled flows in clay materials. *Water Resources Research*, *47*, W05548. https://doi.org/10.1029/2010WR010002

Rüberg, T., & Aznar, J. M. G. (2016). Numerical simulation of solid deformation driven by creeping flow using an immersed finite element method. *Advanced Modeling and Simulation in Engineering Sciences*, *3*(1). https://doi.org/10.1186/s40323-016-0061-0

Rusche, H. (2002). Computational fluid dynamics of dispersed two-phase flows at high phase fractions. *Imperial College*. https://doi.org/10.1145/1806799.1806850

Saif, T., Lin, Q., Butcher, A. R., Bijeljic, B., & Blunt, M. J. (2017). Multi-scale multi-dimensional microstructure imaging of oil shale pyrolysis using X-ray micro-tomography, automated ultra-high resolution SEM, MAPS Mineralogy and FIB-SEM. *Applied Energy*, *202*, 628–647. https://doi.org/10.1016/j.apenergy.2017.05.039

Samarasinghe, A. M., Huang, Y. H., & Drnevich, V. P. (1982). Permeability and consolidation of normally consolidated soils. *Journal of the Geotechnical Engineering Division*, *108*(Compendex), 835–850. https://doi.org/10.1061/(ASCE)0733-9410(1983)109:6(871)

Santillán, D., Juanes, R., & Cueto-Felgueroso, L. (2018). Phase-field model of hydraulic fracturing in poroelastic media: fracture propagation, arrest and branching under fluid injection and extraction. *Journal of Geophysical Research: Solid Earth.*, *123*(3), 2127–2155. https://doi.org/10.1002/2017JB014740

Sellin, P., & Leupin, O. X. (2014). The use of clay as an engineered barrier in radioactive-waste management—A review. *Clays and Clay Minerals*, *61*(6), 477–498. https://doi.org/10.1346/CCMN.2013.0610601

Shen, L., & Chen, Z. (2007). Critical review of the impact of tortuosity on diffusion. *Chemical Engineering Science*, *62*(14), 3748–3755. https://doi.org/10.1016/j.ces.2007.03.041

Sherwood, J. D., & Craster, B. (2000). Transport of water and ions through a clay membrane. *Journal of Colloid and Interface Science*, *230*(2), 349–358. https://doi.org/10.1006/jcis.2000.7100

Showalter, R. (2010). Poro-plastic filtration coupled to Stokes flow. In *Poromechanics III - Biot Centennial (1905-2005)* (pp. 229–241). https://doi.org/10.1201/noe0415380416.ch79

Siddique, J., Ahmed, A., Aziz, A., & Khalique, C. (2017). A review of mixture theory for deformable porous media and applications. *Applied Sciences*, *7*(9), 917. https://doi.org/10.3390/app7090917

Socolow, R., & Pacala, S. (2004). (Talk) stabilization wedges: Solving the climate problem for the next half-century with technologies available today. *Science (New York, N.Y.)*, *305*(5686), 968–972. https://doi.org/10.1126/science.1100103

Song, W., & Kovscek, A. R. (2015). Functionalization of micromodels with kaolinite for investigation of low salinity oil-recovery processes. *Lab on a Chip*, *15*(16), 3314–3325. https://doi.org/10.1039/C5LC00544B

Soulaine, C., Creux, P., & Tchelepi, H. A. (2018). Micro-continuum framework for pore-scale multiphase fluid transport in shale formations. *Transport in Porous Media*, *127*(1), 85–112. https://doi.org/10.1007/s11242-018-1181-4

Soulaine, C., Roman, S., Kovscek, A., & Tchelepi, H. A. (2017). Mineral dissolution and wormholing from a pore-scale perspective. *Journal of Fluid Mechanics*, *827*, 457–483. https://doi.org/10.1017/jfm.2017.499

Soulaine, C., Roman, S., Kovscek, A., & Tchelepi, H. A. (2018). Pore-scale modelling of multiphase reactive flow: Application to mineral dissolution with production of. *Journal of Fluid Mechanics*, *855*, 616–645. https://doi.org/10.1017/jfm.2018.655

S4oulaine, C., & Tchelepi, H. A. (2016). Micro-continuum approach for pore-scale simulation of subsurface processes. *Transport in Porous Media*, *113*(3), 431–456. https://doi.org/10.1007/s11242-016-0701-3

Spearman, J. (2017). An examination of the rheology of flocculated clay suspensions. *Ocean Dynamics*, *67*(3–4), 485–497. https://doi.org/10.1007/s10236-017-1041-8

Sposito, G. (2008). *The chemistry of soils. The chemistry of soils/Garrison Sposito*. Oxford, England: Oxford University Press. Retrieved from https://global.oup.com/academic/product/the-chemistry-of-soils-9780195313697?cc=us&lang=en&

Suzuki, S., Prayongphan, S., Ichikawa, Y., & Chae, B. G. (2005). In situ observations of the swelling of bentonite aggregates in NaCl solution. *Applied Clay Science*, *29*(2), 89–98. https://doi.org/10.1016/j.clay.2004.11.001

Teich-McGoldrick, S. L., Greathouse, J. A., Jové-Colón, C. F., & Cygan, R. T. (2015). Swelling properties of montmorillonite and beidellite clay minerals from molecular simulation: Comparison of temperature, interlayer cation, and charge location effects. *Journal of Physical Chemistry C*, *119*(36), 20,880–20,891. https://doi.org/10.1021/acs.jpcc.5b03253

Terzaghi, K. (1964). Theoretical soil mechanics. *Géotechnique*, *14*(1), 1–13. https://doi.org/10.1680/geot.1964.14.1.1

Tessier, D. (1990). Behaviour and microstructure of clay minerals. *Soil Colloids and Their Associations in Aggregates*, *214*, 387–415. https://doi.org/10.1007/978-1-4899-2611-1_14

Tester, C. C., Aloni, S., Gilbert, B., & Banfield, J. F. (2016). Short- and long-range attractive forces that influence the structure of montmorillonite osmotic hydrates. *Langmuir*, *32*(46), 12,039–12,046. https://doi.org/10.1021/acs.langmuir.6b03265

Tezduyar, T. E. (2001). Finite element methods for flow problems with moving boundaries and interfaces. *Archives of Computational Methods in Engineering*, *8*(2), 83–130. https://doi.org/10.1007/BF02897870

Tournassat, C., Bourg, I. C., Steefel, C. I., & Bergaya, F. (2015). Surface properties of clay minerals. *Developments in Clay Science*, *6*, 5–31. https://doi.org/10.1016/B978-0-08-100027-4.00001-2

Tuković, Ž., & Jasak, H. (2007). Updated Lagrangian finite volume solver for large deformation dynamic response of elastic body. *Transactions of Famena*, *31*(1), 55–70.

Tuller, M., & Or, D. (2003). Hydraulic functions for swelling soils: Pore scale considerations. *Journal of Hydrology*, *272*(1–4), 50–71. https://doi.org/10.1016/S0022-1694(02)00254-8

Tuller, M., & Or, D. (2006). Hydraulic properties of swelling clay-sand mixtures: Microscale modeling and measurements. *Unsaturated Soils 2006* Vol. 40802, 2186–2197. https://doi.org/10.1061/40802(189)185

Van Loon, L. R. (2015). A modified version of Archie's law to estimate effective diffusion coefficients of radionuclides in argillaceous rocks and its application in safety analysis studies. *Applied Geochemistry*, *59*, 85–94. https://doi.org/10.1016/j.apgeochem.2015.04.002

Van Loon, L. R., Soler, J. M., Jakob, A., & Bradbury, M. H. (2003). Effect of confining pressure on the diffusion of HTO,36Cl- and 125I- in a layered argillaceous rock (Opalinus Clay): Diffusion perpendicular to the fabric. *Applied Geochemistry*, *18*(10), 1653–1662. https://doi.org/10.1016/S0883-2927(03)00047-7

Van Loon, L. R., Glaus, M. A., & Müller, W. (2007). Anion exclusion effects in compacted bentonites: Towards a better understanding of anion diffusion. *Applied Geochemistry*, *22*(11), 2536–2552. https://doi.org/10.1016/j.apgeochem.2007.07.008

Van Loon, L. R., Soler, J. M., Müller, W., & Bradbury, M. H. (2004). Anisotropic diffusion in layered argillaceous rocks: A case study with Opalinus Clay. *Environmental Science and Technology*, *38*(21), 5721–5728. https://doi.org/10.1021/es049937g

Vo, G. D., & Heys, J. (2011). Biofilm deformation in response to fluid flow in capillaries. *Biotechnology and Bioengineering*, *108*(8), 1893–1899. https://doi.org/10.1002/bit.23139

Wang, L., Wang, L. P., Guo, Z., & Mi, J. (2015). Volume-averaged macroscopic equation for fluid flow in moving porous media. *International Journal of Heat and Mass Transfer*, *82*, 357–368. https://doi.org/10.1016/j.ijheatmasstransfer.2014.11.056

Weller, H. G., & Tabor, G. (1998). A tensorial approach to computational continuum mechanics using object-oriented techniques. *Computers in Physics*, *12*(6), 620–631. https://doi.org/10.1063/1.168744

Whitaker, S. (2013). Volume averaging of transport equations. *Fluid Transport in Porous Media*, *53*(9), 1689–1699. https://doi.org/10.1017/CBO9781107415324.004